

1-1-1994

A STUDY OF DC PERMANENT MAGNET MOTOR NOISE RELATED TO LINE CURRENT

Candace Rogers Suriano

Purdue University School of Electrical Engineering

Follow this and additional works at: <http://docs.lib.purdue.edu/ecetr>



Part of the [Power and Energy Commons](#)

Suriano, Candace Rogers, "A STUDY OF DC PERMANENT MAGNET MOTOR NOISE RELATED TO LINE CURRENT" (1994). *ECE Technical Reports*. Paper 174.
<http://docs.lib.purdue.edu/ecetr/174>

This document has been made available through Purdue e-Pubs, a service of the Purdue University Libraries. Please contact epubs@purdue.edu for additional information.

A STUDY OF DC PERMANENT MAGNET MOTOR NOISE RELATED TO LINE CURRENT

CANDACE ROGERS SURIANO

TR-EE 94-5
JANUARY 1994



SCHOOL OF ELECTRICAL ENGINEERING
PURDUE UNIVERSITY
WEST LAFAYETTE, INDIANA 47907-1285

**A STUDY OF DC PERMANENT MAGNET MOTOR NOISE
RELATED TO LINE CURRENT**

Candace Rogers Suriano

Purdue Elecme Power Center
School of Electrical Engineering
Purdue University
1285 Electrical Engineering Building
West Lafayette, IN 47907-1285

December 1993



ABSTRACT

Lightweight, compact and inexpensive DC permanent magnet motors are well suited for low cost high production use in industry. Unfortunately, the audible noise emanating from these motors can cause a false negative perception of the motor's quality. In cars, for example, fan motor noise can be a nuisance. The objective of this **thesis** is to examine the **connection** between motor noise and the line current wave form for a specific four pole DC **permanent** magnet motor. It is further concerned with **identifying** the **underlying** factors which influence the line current ripple. An audible noise to motor current transfer function is determined from test measurements and compared with a the **mechanical** transfer function measured for the motor and for the motor in the fan scroll **assembly**. The inductance, which is a factor in the shape of the **current** ripple, is **computed** from theoretical and empirical inductance functions. Next a sequence of progressively more complex models is used to compute the current wave form. Arcing and commutation mechanisms are included in the most sophisticated of the models.

TABLE OF CONTENTS

	Page
LIST OF TABLES	vi
LIST OF FIGURES	vii
ABSTRACT	ix
CHAPTER 1. INTRODUCTION.....	1
Transformer Noise Research	1
Motor Noise Research	2
Review of Modeling Techniques	3
DC Motor Noise Sources	4
DC Motor Operation	6
Preview	7
CHAPTER 2. TRANSFER FUNCTION RELATIONSHIPS BETWEEN AUDIBLE NOISE AND MOTOR CURRENT	11
Experimental Apparatus	11
Experimental Method	12
Motor Sound to Current Transfer Function	14
Electrically Excited DC Motor Noise	16
CHAPTER 3. INDUCTIVE COUPLING OF ARMATURE COILS IN PERMANENT MAGNET DC MOTORS.....	26
Individual Coil Self Inductance	26
Mutual Inductance Between Individual Coils	27
Ideal Mutual Coil Coupling	27
Experimentally Obtained Mutual Coupling.....	30
Equivalent Inductance of Coil Assemblage.....	31
Use of Connection Matrices	32
Calculation of Equivalent Inductance Values.....	35
Reduction of Experimental Data	36
Approximations for the Equivalent Inductance.....	37
Effect of Inductance Variation and Mutual Coupling on Noise	38

	Page
CHAPTER 4. SIMULATION OF LINE CURRENT	48
DC Permanent Magnet Motor Models	48
Preliminary Permanent Magnet Motor Models	49
Average Value Model	49
Time Varying Model	50
Time Varying Model with Position Dependent Inductance	51
Mutually Coupled Arcing Model	51
Brush Width Variation	53
Motor Speed Variation	54
Brush Shift Variation	54
Further Research	55
CHAPTER 5. CONCLUSIONS AND FUTURE RESEARCH	67
Research Summary	67
Conclusions	68
Future Research	68
LIST OF REFERENCES	70



LIST OF TABLES

Table	Page
3.1 Relative Location of Armature Bars and Coils.....	33

LIST OF FIGURES

Figure	Page
1.1 One Coil DC Permanent Magnet Motor.....	8
1.2 Permanent Magnet Magnetic Flux Path	8
1.3 0" Brush Shift Current Wave Form	9
1.4 -15" Brush Shift Current Wave Form.....	9
1.5 Motor Cross-Section	10
2.1 Experimental Apparatus for Sound to Current Transfer Function	18
2.2 Transformer Sound Output for Sine Wave Current Input	19
2.3 Transformer Sound Output for Pseudo-Square Wave Current Input with Harmonics	19
2.4 Transformer Sound to Current Transfer Function	20
2.5 Pendulum Mode Shapes	20
2.6 Motor and Fan Scroll Assembly Oscilloscope Output for Sine Wave Current Input.....	21
2.7 Motor and Fan Scroll Assembly Oscilloscope Output for Square Wave Current Input.....	21
2.8 Motor and Fan Scroll Assembly Sound to Current Transfer Function	22
2.9 Mechanical Transfer Function for Motor Showing 500 Hz and 700 Hz Peaks	22
2.10 Mechanical Transfer Function for Motor Showing 3200 Hz and 4900 Hz Peaks	23
2.11 Mechanical Transfer Function for Motor Showing 700 Hz and 3200 Hz Peaks	23
2.12 Mechanical Transfer Function for Motor and Fan Scroll Assembly Showing 4400 Hz Peak	24
2.13 Mechanical Transfer Function for Motor Showing 2490 Hz and 4900 Hz Peaks	24
2.14. Mechanical Transfer Function Experimental Apparatus.....	25
3.1 Coil Self Inductance Versus Coil Position	39
3.2 Average Coil Self Inductance Versus Coil Number	39
3.3 B-H Curve for Air and Magnet Material	40
3.4 Two Coils Embedded in Armature Within Case	40

Figure	Page
3.5 Calculated Mutual Inductance	41
3.6 Flux Distribution from Primary Coil	41
3.7 Mutual Inductance: Empirical for Case Without Magnets Vs. Calculated	42
3.8 Angular Relationship Between Magnets, Brushes, and Commutator	42
3.9 Four Brush Circuit Configurations	43
3.10 Self Inductance of "a" Coil for Shorted Condition	44
3.11 Self Inductance of "b" Coil for Shorted Condition	44
3.1 Experimental Self Inductance of "a" Coil for Non-Shorted Condition	45
3.131 Resultant Flux Paths	45
3.141 Experimental Mutual Inductance of "a "and"b" Coils for Shorted Condition	46
3.15 Magnet Permeance Effects on Mutual Coupling	46
3.16 Magnet Saturation Effects on Mutual Coupling	47
3.17 Correlation of L_{ab} Equation and Experimental Data	47
4.1 Stationary Circuit Model	56
4.2 Stationary Circuit Model Current Output	56
4.3 Circuit for Noncommutating Time Varying Model	57
4.4 Circuit for Commutating Time Varying Model	57
4.5 Time Varying Model Program Current Output	58
4.6 Measured Line Current	58
4.7 Line Current Predicted Using Position Dependent Inductance	59
4.8 Mutually Coupled Commutating Circuit	59
4.9 Unstable Commutation Arcing Model	60
4.10 Stable Commutation Arcing Model	60
4.11 Commutation Arcing Model Line Current Prediction	61
4.12. Optimal Brush Shift for Various Brush Widths	61
4.13 Line Current Wave Form Change with Brush Width Variation	62
4.14. Commutating Current Wave Form Change with Brush Width Variation	63
4.15 Arc Change with Brush Width Variation	64
4.16 Line Current Change with Motor Speed Variation.....	64
4.17' Commutating Current Change with Motor Speed Variation	65
4.18 Optimal Brush Shift Change with Motor Speed Variation	65
4.19 Line Current Wave Form Change with Brush Shift	66
4.20 Commutating Current Wave Form Change with Brush Shift	66

CHAPTER 1. INTRODUCTION

Noise can be a problem with any piece of electrical equipment. From transformers to DC **motors**, industry is always looking for economical ways to **decrease** the level of emitted acoustic noise and to increase the perceived quality level of electrical devices. **Electromagnetic** interactions produce noise in rotating machines and transformers. This thesis details the relationship between current and noise for a small DC motor. It then **examines** relationships between machine parameters and current wave forms for this motor. Transformer noise is discussed in order to introduce the study of noise in electromechanical devices.

Transformer Noise Research

Large and small AC transformers are the subjects for emitted acoustic noise research and development [I-13,291 due to laws mandating quieter power distribution transformers and because of a desire to increase the quality and marketability of transformers. Transformer noise originates from the periodic cycling of electromechanical forces in the transformer. These forces cause the windings, core, and case enclosing the transformer to move with respect to one another. **Magnetostrictive** forces also cause the core to vibrate [9]. These vibrations result in radiated audible noise. Transformer noise levels are checked with multiple transducers and various types of signal processing.

Sound intensity measurements, [6-8], are made using two closely spaced, phase matched, pressure sensitive microphones to determine a sound vector. Unlike conventional sound pressure techniques, these measurements can **determine** and rank **order** noise sources from operating equipment even when there is background noise. Conventional techniques necessitate anechoic chambers and low levels of background noise to determine the amount of sound power emanating from a source.

Transformer decibel levels are weighted with the A-scale to **determine** the level of **loudness** and irritation to the human ear. This scale attenuates very **low** and very high

frequency sounds which are difficult to hear and amplifies mid range frequencies. A-scale: weighted readings are denoted as **dBA** instead of dB. In this way **transformer** noise can be judged by its effect on humans [9].

Noise from large transformers is attenuated by up to 25 dB in the field using large and expensive sound dampening enclosures [10,12]. To determine the need for sound dampening enclosures before a substation or a transformer is built, **sound** levels around substations can be predicted using commercial programs [13,29]. One transformer program uses a finite element routine called Flux **Meca** that takes into account electrical and mechanical reactions. A substation program considers the noise emitted by the transformer and its relationship to **all** the surrounding buildings and **objects** to determine the projected substation neighborhood noise level.

Motor Noise Research

Motors are used in every facet of modern life. As the public demands a quieter environment, the emitted noise and vibration levels of motors must **decrease** [14-28]. Lightweight, compact, and inexpensive DC permanent magnet motors are increasingly being used in industry. In the automotive industry, they are used extensively to drive fans, windshield wipers, antenna lifts, and power windows. In cars, fan motor noise can be a nuisance and a quality defect. Active noise suppression, where speakers are used to cancel noise emanating from annoying sources [31], would be very effective but expensive. Mechanical dampers, such as rubber boots, reflecting enclosures such as used with refrigerator compressors, and adsorptive silencers [14] around the motor, lower the level of transmitted noise. Unfortunately, mechanical dampers aren't always economical or adequate and they are almost always bulky.

Signature analysis can be used in determining where motor noise originates [15,16]. The **frequency** spectrum is used to identify whether the noise in an **induction** motor is of magnetic origin or from the windage [16]. In a vacuum cleaner, **signature** analysis can pin down whether the noise is due to the airflow, motor or surrounding structure [15].

Laser holography can be utilized to do a modal shape analysis. It **has** been used to **determine** the complex mode shapes of an automobile engine [17]. **After** the vibration analysis is **carried** out, mass can be added to or removed from the motor case in such a way as to eliminate imitating noise frequencies by eliminating the corresponding mode shape. Noise levels are reduced by decreasing vibration, because the noise is related to the level of vibration [18].

Current discontinuities resulting in an excess of harmonic frequencies can cause vibrations and noise problems [19]. Papers [20-25] detail different methods employing power electronics to impact non-fundamental current harmonics in the **audible** frequency **range** to reduce the level of noise emanating from both AC and DC machines.

Mechanical noise transmissions can be reduced by isolating or dampening the noise transmission path [26] or source of noise. Noise transmission can **be** decreased by changing the transmission path's stiffness or damping. One way the noise transmission path can be changed is by utilizing low noise bearings and lubricants [27]. Low noise ball bearings have smaller changes in rigidity during bearing rotation than standard bearings, resulting in smaller system oscillations and less instability that can lead to vibration and noise. Low noise lubricants have more damping than standard lubricants. **Particularly** effective are fluoroester based oils

DC machines can have their vibrations actively suppressed by adding extra coils to provide magnetic fields equal and opposite to those normally produced by the **machine**[28]. However this technique is too expensive to be feasible when dealing with low cost, high volume, compact DC motors.

Review of **Modeling** Techniques

Many authors have contributed to the modeling and analysis of DC motor devices and **motors** with permanent magnets [30,32-35,37-42]. Much of the published research on DC permanent magnet motors is devoted to the shape of the magnetic field and its influence upon the voltage, torque and current of the motor. Research devoted to the critical aspect of the motor brush design is very important, but generally proprietary.

Brushes for DC motors are generally made out of a carbon graphite compound. For very small DC micromotors the brushes are usually carbon steel springs, to maintain strength in very small size. Carbon brushes are generally compounded with various alloys to increase current flow, decrease frictional coefficients, strengthen the brush, lengthen the life of the brush and decrease the amount of commutator arcing. For **example**, copper and graphite are both used to increase the current carrying capacity of a **brush**. Graphite reduces the frictional coefficient between the brush and the **commutator** bars, but graphite reduces the brush life span. Copper **increases** the life of the brush and strengthens it, but also increases the frictional **coefficient** between the brush and the commutator bars.

By examining the magnetic field shape for a DC permanent magnet micromotor, such as is used on a floppy disk drive, Pawlak [30] from the GM Research Laboratories **determined** that a rectangular field shape would eliminate the ripple on the induced **voltage** and therefore eliminate torque pulsation.

Since current and its harmonics are so closely related to the internal forces, and hence the noise which motors produce [20-25], modeling of the electric circuit is an important part of predicting the noise level of a motor. Modeling **allows** the current wave form to be predicted even before the motor is built. The more harmonics in a **current** wave form, the noisier the motor.

Using the armature reaction, field flux, magnetic saturation, and mutual interaction between the armature and field flux, for a separately excited DC motor, Suzuki [32] determined that the transient response of a conventional DC motor model was improved, but **not** the steady state case. This new model gave insight into the transient armature reaction of a DC separately excited motor.

DC permanent magnet motors have been simulated using a detailed circuit model by Suriano [42]. This model was very accurate in predicting the wave forms of the current, particularly the effects of commutation.

Modeling of DC machines flux linkages can not be accomplished without accurate measurement of leakage inductances and nonlinear magnetic parameters. Ramshaw [37] showed that by measuring the voltage, current and resistance of the coils and numerically integrating the quantities, the flux linkage of the coil can be determined for a coil. By subtracting the self linkage of the coil from the flux linkage calculated, the leakage inductance can be determined. This nonlinear leakage inductance value can now be used in a model.

Nady Boules in conjunction with other authors has written many papers on DC permanent magnet machine modeling [33,39,40,38,34,35]. In these papers he develops **expressions** for the field shapes, and goes into a model to predict current, torque and voltage for small DC permanent magnet machines.

DC Motor Noise Sources

DC motor noise originates from mechanical and electrical sources as well as from an interaction between the electrical and mechanical systems. The noise from a DC permanent magnet machine is mainly from the vibration of the mechanical components of the machine. Shaft bearings can cause vibration and noise due to misalignment,

improper lubrication, loose bearings, and high friction sintered bearing material. Brushes are a major source of noise. The biggest noise spike from a DC motor occurs at the slot frequency of the motor. Brush noise can be decreased by finding a brush compound with a lower coefficient of friction and by **optimizing** (usually increasing) the brush spring constant to decrease the amount of motion the brush makes perpendicular to the brush slot [43]. Also related to the brush noise is the surface finish of the commutator bars, whether the brush can move freely in the brush slot, and the spacing of the commutator bars. There are other sources of mechanical noise in a DC motor, but the primary sources are the brushes and the bearings. Noise generated by brushes and commutator are transmitted and amplified by the case and structure surrounding the motor. Therefore, some noise components can be decreased by changing the mechanical structure of the motor case.

Electrical sources of vibration are not as significant sources of vibration as the mechanical system of the DC machine. However, once the mechanical system has been optimized, altering the electrical system to reduce vibrations produces a much quieter motor. Arcing between commutator bars can cause noise and damage to the commutator bar surface. Arcing is due to the potentials which are developed as armature current rapidly changes during commutation. As the rotating coil is energized in the magnetic field, the permanent magnets on the case are attracted to the coil on the rotor causing a deflection of the motor case resulting in vibration of the case and rotor coils. The rotor laminations vibrate magnetostrictively and with respect to one another in the changing magnetic field resulting in an barely audible hum emanating from the laminations. This vibration can be reduced by using a lamination coating with a higher damping coefficient, although for small fractional horsepower machines this is generally unwarranted. Some of the electrically caused vibration is transmitted to the case of the machine and can be substantially reduced by changing the mechanical structure of the case.

Cogging torque also causes vibrations in DC machines. Cogging occurs when the reluctance of the permanent magnet flux path changes. A small reluctance torque attempts to prevent the armature from rotating as the rotor teeth provide the minimum reluctance path to the magnet's flux. To reduce **cogging**, the teeth of the rotor are skewed.

DC Motor Operation

A simple one coil permanent magnet DC motor is described in Figure 1.1. There are two permanent magnets attached to the thick steel case of the machine. The magnet on the top of the figure has a south pole pointing away from the armature and the magnet on the bottom has a north pole pointing toward the armature. This provides a complete magnetic circuit as shown in Figure 1.2. Magnetic flux in this circuit flows through the DC motor's case, which is thick steel because it must **carry** the flux from the permanent magnets. Current flows into the coil through the brushes into the rotor which make sliding contact with the commutator bars. Current in the rotor coil creates a magnetic flux that produces a torque when it interacts with the magnetic flux of the magnets mounted on the case of the motor. As the armature rotates, the brush bridges the space between the commutator bar segments shorting the coil connected between the two adjacent segments. A large $L di/dt$ voltage, usually towards the end of commutation, causes an arc between the commutator bars. Coil current is reversed when the rotor continues on its journey and the torque direction is preserved. The motor of Figure 1.1 is not a practical motor because it can not produce enough consistent starting torque. A practical motor has more coils and commutator bars, but not necessarily more magnets.

In order to lower the amount of arcing between the commutator bars, the brushes are shifted. With no brush shift, or a brush shift of 0 degrees, In this position the induced current in the commutating coil produces flux which adds to the permanent magnet field and results in fair to poor commutation. The line current for this condition is shown in Figure 1.3. A negative brush shift moves the location of the brushes in the direction opposite rotation. In this way, the magnetic field of the coil subtracts from the magnetic field of the permanent magnets before the motor commutates and the coil current is more sinusoidal as shown in Figure 1.4. For a particular loading, shifting the brushes can eliminate much of the arcing between commutator bars and some or all of the coil current spikes.

The armature and case of the specific four pole DC machine that is studied in this thesis is shown in Figure 1.5. There are twelve coils wound around the armatures twelve teeth. Each coil is wound around three teeth in order to make each current path magnetically independent with the other 3 current paths. Four poles necessitate four permanent magnets attached to the steel case.

Preview

The objective of this thesis is to examine the electromechanical sources of undesirable vibrations both through modeling and through empirical data for a particular permanent magnet DC motor. AC transformers, which are related to DC motors on an elementary level, are also briefly examined. All the stresses that occur in a small transformer also occur in a DC motor in a more complex setting. Periodic cycling of magnetomotive force in the transformer cause the windings, core, and case enclosing the transformer to move with respect to one another. Magnetostrictive forces cause additional core motion [9].

Chapter 2 includes empirical data relating the current wave form characteristics to the audible noise from the four pole DC motor and from a transformer. In Chapter 3, the mutual inductance values are measured and calculated for the DC permanent magnet four pole motor. These data are transformed from a four terminal form to an equivalent two terminal form using connection matrices. Chapter 4 contains four different models of the motor and a comparison of the number of parameters needed to form each model. Conclusions and recommendations are presented in Chapter 5.

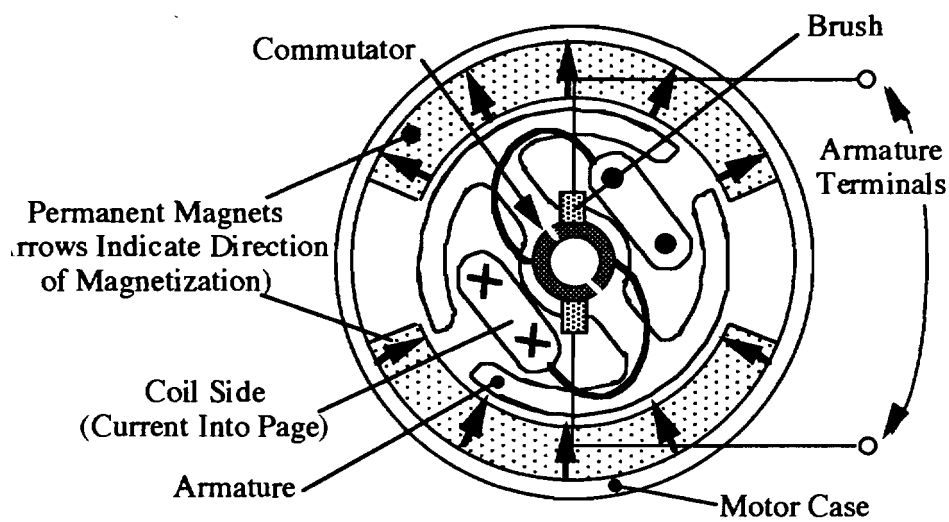


Figure 1.1. One Coil DC Permanent Magnet Motor

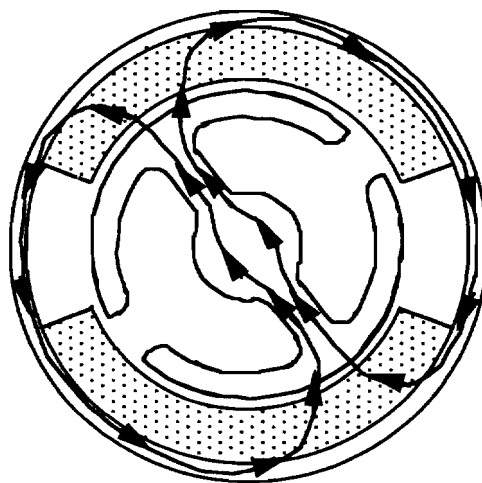


Figure 1.2 Permanent Magnet Magnetic Flux Path

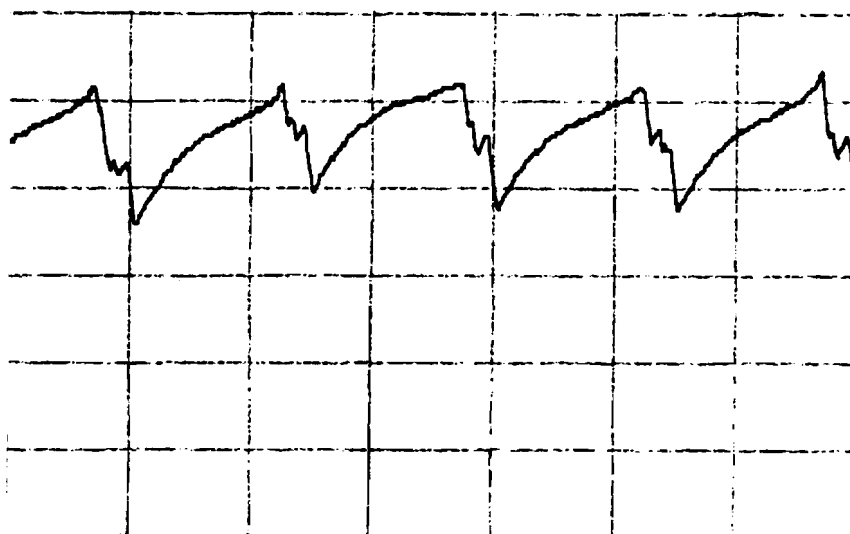


Figure 13 0° Brush Shift Current Wave Form

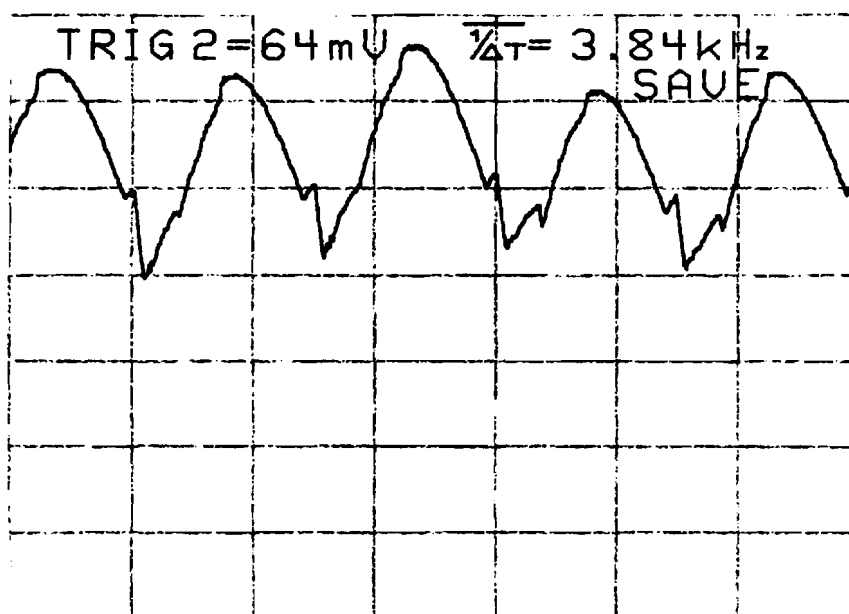


Figure 1.4 -15° Brush Shift Current Wave Form

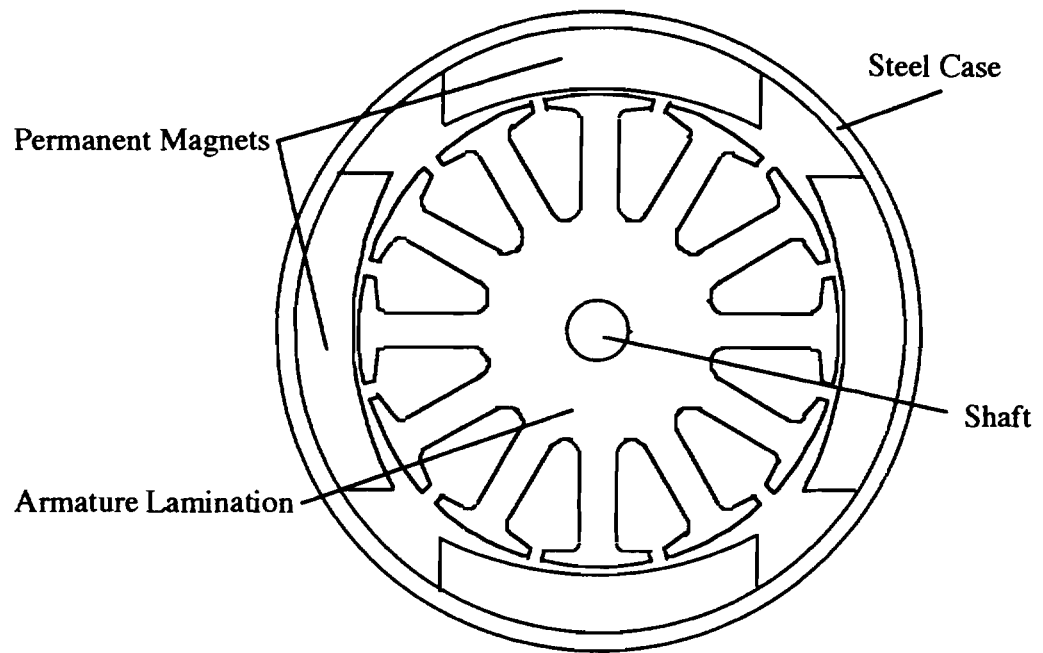


Figure 1.5 Motor Cross-Section

CHAPTER 2. TRANSFER FUNCTION RELATIONSHIPS BETWEEN AUDIBLE NOISE AND MOTOR CURRENT

Initial testing of the four pole DC permanent magnet motor involved injection of alternating current into the stationary armature through the motor terminals. It was observed that the most disturbing noise occurred when current wave forms having higher harmonics, such as a square wave, were fed into the armature. Yet, a sine wave current with the identical amplitude input to the same machine produced a much less noticeable noise. This observation served as the impetus for finding a transfer function between the current input to the four pole DC permanent magnet machine and its sound output.

In many electrical engineering problems it is possible to identify a transfer function between critical input and output variables by constraining other pertinent variables. This chapter examines the relationship between sound output and current input first for a small transformer as a demonstration and next for a four pole DC permanent magnet machine. It then compares mechanical transfer functions of the motor case with the harmonics indicated by the sound output to armature current transfer function obtained for the machine.

Experimental Apparatus

Figure 2.1a shows a representation of the experimental apparatus used to obtain the sound output, current input transfer function. A high impedance microphone was connected to an amplifier circuit to boost the microphone output signal by a gain of 10,000. Voltage output by this signal was input to a digital storage oscilloscope. Current input to the motor from a signal generator was transformed from low current, high voltage to high current, low voltage by a transformer. Current was measured by a current sensing probe which was also connected to the digital storage oscilloscope. The digital storage oscilloscope was connected to a plotter to provide a hard copy of the data. An alternate arrangement, shown in Figure 2.1b, utilized a servo-amplifier to provide square wave current wave forms to the motor.

A bamer consisting mostly of a medium density closed cell foam surrounded the motor and fan scroll assembly with the microphone protruding through a low density expandable polystyrene (eps) block. The foam bamer helped to minimize interference from sound waves reflecting off the walls of the room.

For the transformer tests, interaction between the device and the table where the experiment was performed was minimized by suspending the transformer from a spring on a stand placed on a piece of medium density closed cell foam. For the motor testing, interaction between the device and the table was minimized by putting the motor or motor and scroll assembly on a low density **eps** base.

Normally sound measurements are best conducted in an anechoic chamber. An anechoic chamber does not have any experimentally significant ambient noise levels. It is constructed in such a way as to minimize the reflected sound waves in the room and to make sure that there are no standing waves set up in the chamber which can ruin the experiment. This experiment however, was run in a laboratory with painted cinder block walls and wooden floors. Air vent noise was muffled by covering the vent with a plastic sheet. Ambient noise levels were minimized by carrying out the experiments when the building noise levels were lowest during vacation, at night and on weekends. These precautions along with the **barriers** of closed cell foam and low density eps insured repeatability of noise to current transfer function ratios as verified by duplicate measurements made on different days.

Experimental Method

An audible sound to line current transfer function is characterized by sine wave sound output at the same frequency as a sine wave current input. This requires the relationship between current and sound to be linear at each frequency. If the input current sine wave is varied, the microphone output must vary proportionally. Transfer functions are usually obtained by approximating the impulse response by the input of a narrow pulse. This method was not possible for the DC motor. It was not practical to create a current pulse input to the motor of sufficient energy and short duration. Even a 5 Amp spike lasting for 4 micro seconds did not provide enough power, so the sine wave method was adopted. In addition to sine wave inputs, the sound output due to square wave current wave forms was also examined.

A sine wave current wave form was fed into the transformer which was suspended on a spring to minimize the amount of interaction between the table and the transformer.

Boosted voltage output from the microphone was then examined and stored on the digital storage oscilloscope. The wave form magnitudes were recorded and plotted, an example of which is shown in Figure 2.2. To form the transfer function, the ratio of the amplitude of the boosted voltage output to the amplitude of the current wave form at each frequency was plotted. At some of the frequencies, various amplitudes of the sine wave current input to the transformer were studied in their relationship to the amplified sine wave output of the microphone to insure that the relationship between the input and the output was linear at that frequency. It was assumed from this testing that linearity could be generalized to all frequencies.

Unfortunately, because of the dynamics between the signal generator and the transformer circuit it was not possible to impress a square wave current input to the transformer. However, Figure 2.3 shows a distorted current wave form and the resulting sound wave form. It is easy to recognize that the fundamental frequency of the output occurs at the fundamental frequency of the input. Figure 2.4 shows the resulting sound to current transfer function for the transformer.

If a rigorous evaluation of the effect of the noise on humans was conducted, the sound output would be put in decibel form and the data would be weighted by the **A**-scale. The units of the sound would then be **dbA** and would correlate directly to the amount of noise perceived by a typical human ear. In this cursory evaluation there are peaks observed in the soundcurrent transfer function at approximately 1100 and 5600 Hz. At these frequencies the transformer noise was irritating to the experimenter. In order to reduce the amount of noise the transformer produces, these harmonics should be filtered from the input current.

Operating the transformer without its steel case lowered the noise to an inaudible level. This information implies that electrically induced excitation leading to vibration of the case of the transformer caused the audible noise. So, these irritating frequencies could be changed or eliminated by altering the case structure or mechanically damping the case with some type of polymer or mass. The natural mode frequencies of the transformer case should correspond to the frequency peaks in the soundcurrent transfer function.

A natural vibration mode of an object is the way an object tends to move when excited at or near a certain frequency. In a mechanical transfer function the natural vibration modes show up as peaks at the mode frequencies. If an object is excited at or near a natural frequency of the object, the object's motion increases and the potential for noise problems expands especially if a flat surface on the object is involved. An

excellent example of mode shapes and frequencies is a pendulum consisting of a weight suspended by a chain. If the pendulum swings at a certain frequency it moves with a back and forth motion as shown in Figure 2.5a. If the pendulum is swung faster it starts to deviate from the gentle back and forth motion to one similar to that shown in Figure 2.5b where the chain deforms.

Motor Sound to Current Transfer Function

A transfer function for a motor and fan scroll assembly shown in Figure 2.1 was evaluated using the aforementioned procedure. Some points on the transfer function for the motor by itself were also taken. Data was taken for the motor and fan scroll assembly up to the 10th harmonic of the slot frequency of the motor. The slot frequency is the fundamental frequency of the armature current during operation and is equal to the number of slots of the commutator times the rotational frequency of the motor. Figure 2.6 shows sample output for the motor and fan scroll assembly. It is evident from these graphs that the transfer function is linear. A sine wave current input produces a sine wave sound output at the same frequency. By repeating some experimental values at various current levels, it was observed that the transfer function at those frequencies did not change and that the values obtained varied within reasonable experimental error. A square wave current input to the motor and fan scroll assembly shown in Figure 2.7 illustrates the result of a motor's response to harmonics. The fundamental sound wave output is at the fundamental frequency of the current input. Noise due to harmonics from the current input are added to the output, weighted by the transfer function at the harmonic frequency and appear superimposed on the fundamental output sound frequency. Since the response of the motor is different for each of the **harmonics**, some are amplified and some attenuated.

Figure 2.8 shows the sound to current transfer function for the motor and fan scroll assembly. Peaks in the transfer function occur at approximately 400, 500, 700, 2400, 3200, 4400, **4900**, and **5700** Hz even when the experiment was repeated with the microphone in a different position. At these frequencies the subjectively observed noise level of the motor and fan scroll fan assembly was **irritating**. Noise observed at these peaks corresponds to natural resonances of the assembly.

There was no audible noise observed when the armature, having been removed from the motor case and magnets, was excited by various current wave forms. This points to the interaction between the armature excitation and the case with the magnets. As the

various coils are energized by current or by magnetic coupling through mutual inductance, the magnetic field produced by the coil attracts or repels the permanent magnets in the case. In this way, energy is transferred directly from the armature to the steel case. Therefore, it is reasonable to assume that mechanical excitation of the case should incur a similar response as electromagnetic case excitation.

Figures **2.9-2.13** are plots of mechanical transfer functions taken at Hemck Labs. These transfer functions are produced by measuring vibrations caused by mechanical pulse excitation of the assembly by striking it with a hammer. Vibration due to a steel tipped hammer tap was measured by an accelerometer at various spots on the motor case. Mechanical transfer functions were taken by applying the input at the case rear bearing area and the flange and then measuring vibration response on the mounting flange as shown in Figure **2.14**, Interaction between the table where the experiment took place and the motor or motor and fan scroll assembly were minimized by placing the devices on a 4 inch thick block of high density closed cell foam. Data was taken using an uncalibrated accelerometer affixed with bee's wax to the motor to record response created by a steel tipped hammer. Mechanical transfer functions were created by processing transducer output from the hammer by an FFT (fast **fourier** transform). Accelerometer measurement of vibration was filtered by a **Hanning** window without zero padding and divided by the similarly processed input signal to **determine** the transfer function.

Mechanical transfer functions shown in Figures **2.9-2.13** have coincident peaks with the sound output to current input transfer function measured for the motor and fan scroll assembly shown in Figure **2.8**. Above the frequency shown on the graphs of the mechanical transfer functions, not enough power was transferred from the hammer to the motor to produce an accurate mechanical transfer function.

Even though the sound output to current input transfer function was developed for the non-rotating motor, it is logical to assume that the modes correspond to those which are present when the armature rotates. The movement of the magnets in response to current fluctuations produced as a result of motor operation result in case vibrations which excite the same natural frequencies as those found with the mechanical and current inputs.

The mechanical transfer function shown in Figure **2.9** relates a mechanical input to the side of the flange, with resulting vibrations on the mounting flange of the motor. This transfer function has peaks at the same frequency as those found **with** the current response at 500 and 700 Hz. Figure **2.10** shows a mechanical transfer function from the

motor that was taken by applying force input on a different section of the flange side while measuring the output at the same point on the mounting flange. Figure 2.10 peaks at 3200 and 4900 Hz match with the sound output to current input transfer function peaks. Coincident peaks between the sound output to current input transfer function and the mechanical transfer function for input on the top of the flange and output on the mounting flange occur at 700 and 3200 Hz as shown in Figure 2.11. Figure 2.12 is a mechanical transfer function taken by impacting the case rear bearing area on the motor and fan scroll assembly, it has a peak at 4400 Hz that coincides with one on the sound output to current input transfer function. A mechanical transfer function taken by applying force on the bearing area of the flange has peaks at 2400 and 4900 Hz that correspond to similar peaks on the sound output to current input transfer function in Figure 2.13.

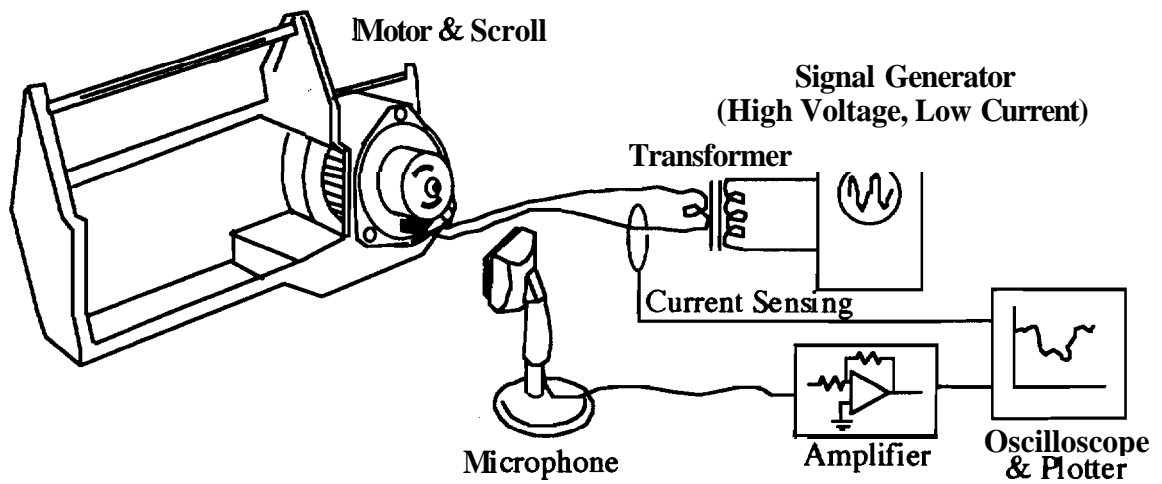
The agreement of the peaks measured using two different transfer function techniques points out how the electrical and mechanical systems interact. Electrical excitation excites some of the mechanical modes of the machine. Modes are excited when energy is transferred to the structure at certain points on the motor. Only two of the peaks, at 400 Hz and 2400 Hz, from the sound output to current input transfer function did not show up clearly on one of the various mechanical transfer functions that were obtained using the equipment at Hemck Labs. One explanation for this is that the specific impact and sensing points chosen were not comprehensive in their coverage. Additionally, below a certain critical frequency, the peak values on the mechanical transfer function can vary by $1/\omega$ to $1/\omega^3$ times those on the sound versus frequency transfer function [44].

Electrically Excited DC Motor Noise

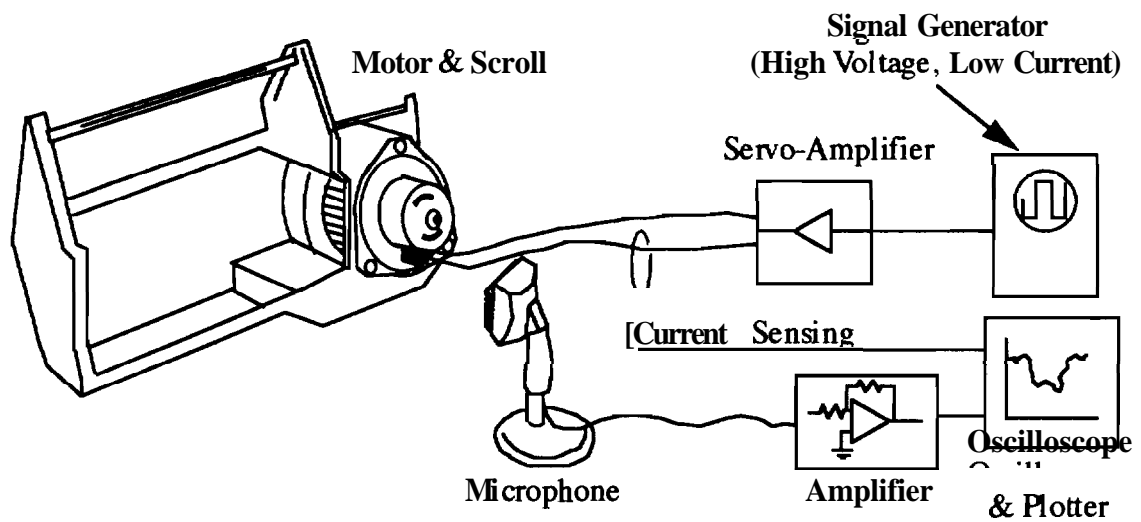
DC motor noise originates from electromagnetic stimulus of the mechanical structure as shown by the correlation between the mechanical transfer functions and the sound output to current input transfer function. Audible noise originating in the electrical system of the motor corresponds to the wave form of the current input to the machine. The more harmonics in the wave form, the noisier the machine.

Wave form harmonics are produced by discontinuities due to commutation. During commutation only two-thirds of the conductors contribute to the resistance, inductance, and back emf that is seen at the terminals. Commutation affects current harmonics because the mutual coupling from the commutating coils transfers energy from the wave

form in those coils to the other coils and because of the sudden switching of coils in the armature circuits. Therefore in order to rigorously study the electrically produced noise in the motor, the mutual coupling of the coils is examined in chapter 3.



(a) Test Configuration for Sine Wave Input



(b) Test Configuration for Square Wave Input

Figure 2.1 Experimental Apparatus for Sound to Current Transfer Function

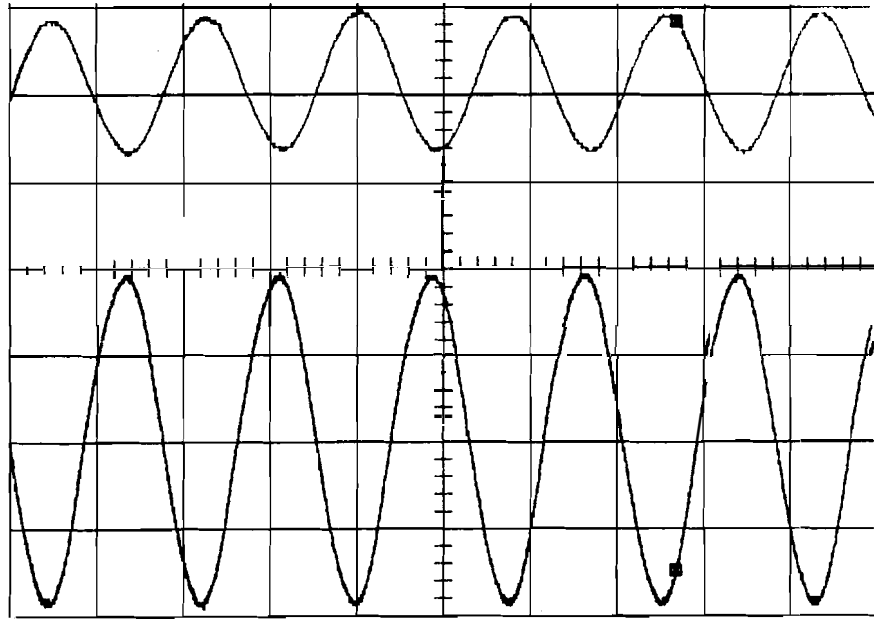


Figure 2.2 Transformer Sound Output for Sine Wave Current Input

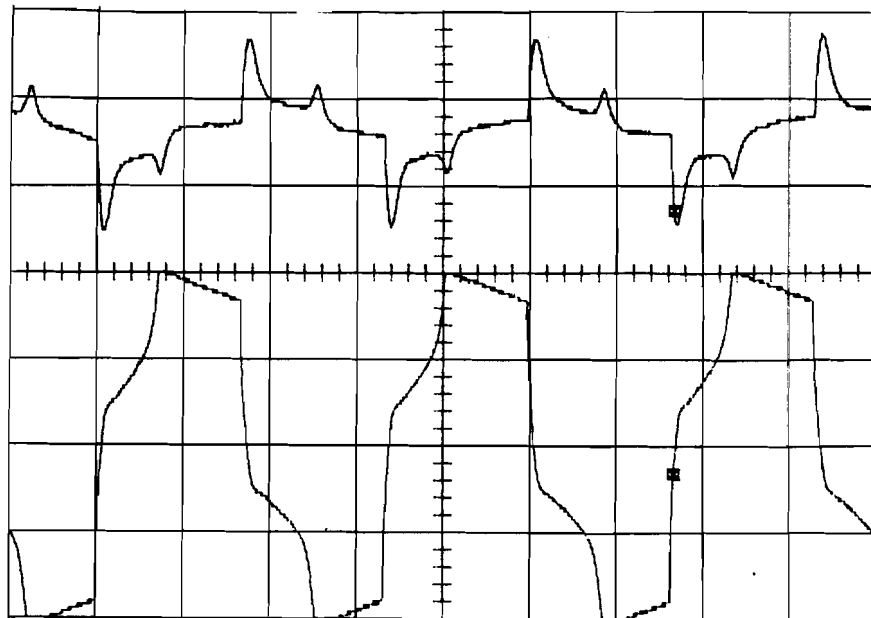


Figure 2.3 Transformer Sound Output for Pseudo-Square Wave Current Input with Harmonics

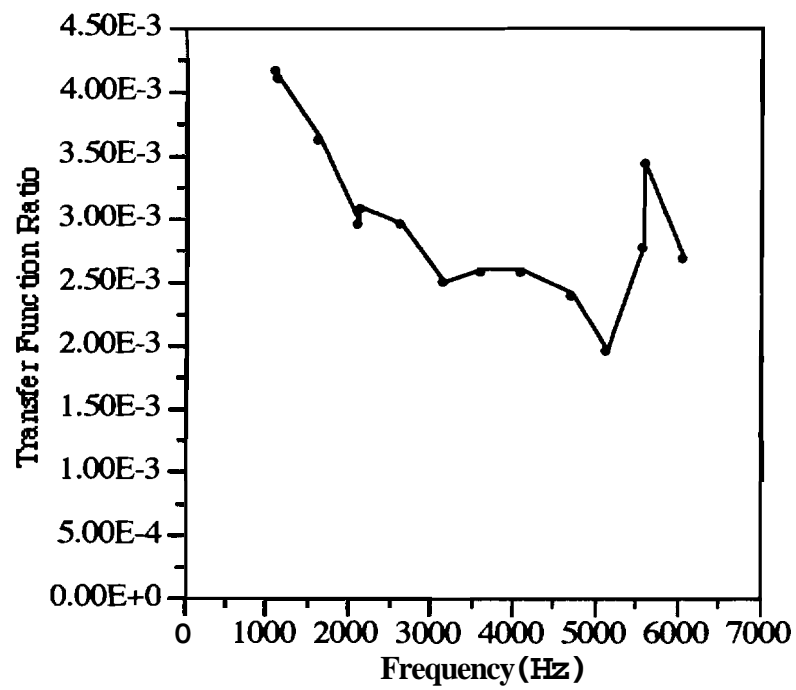


Figure 2.4 Transformer Sound to Current Transfer Function

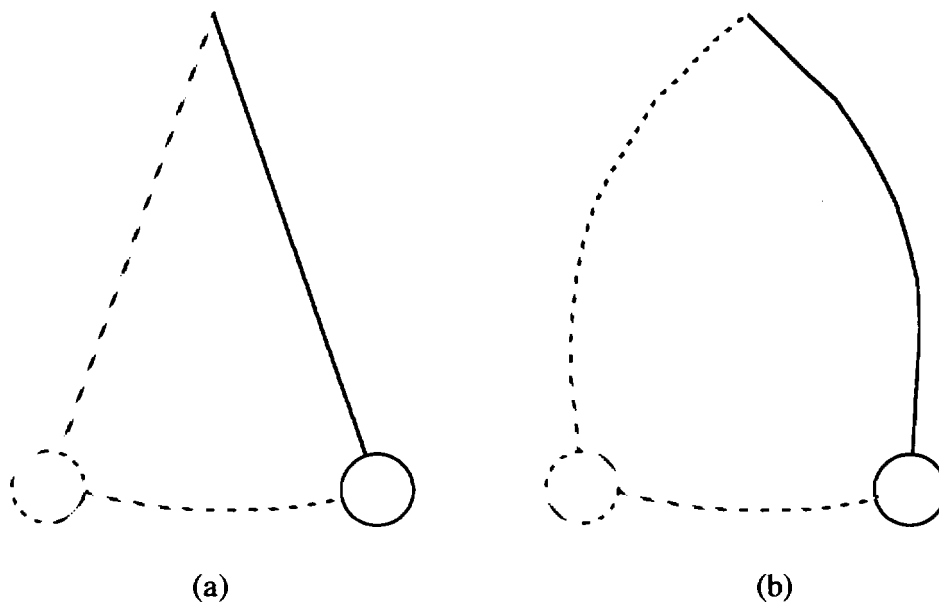


Figure 2.5 Pendulum Mode Shapes

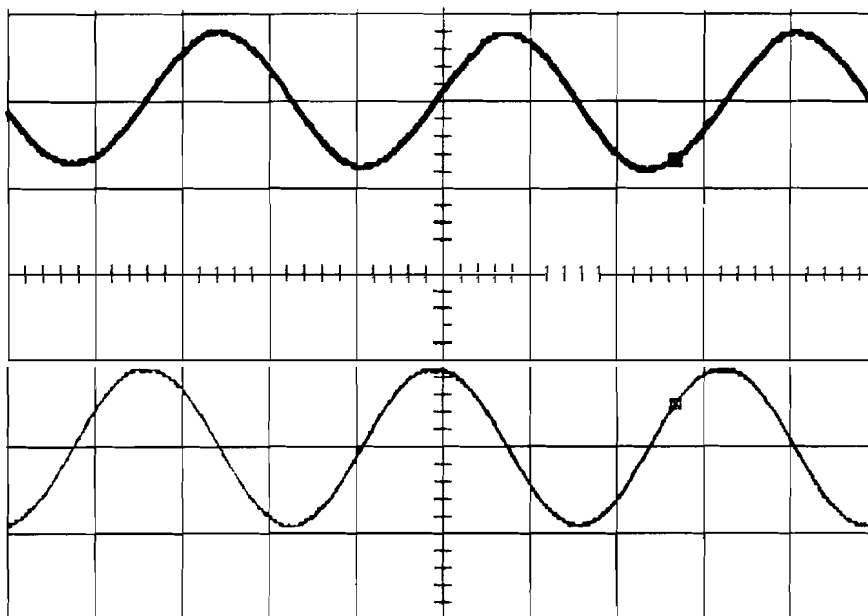


Figure 2.6 Motor and Fan Scroll Assembly Oscilloscope Output for Sine Wave Current Input

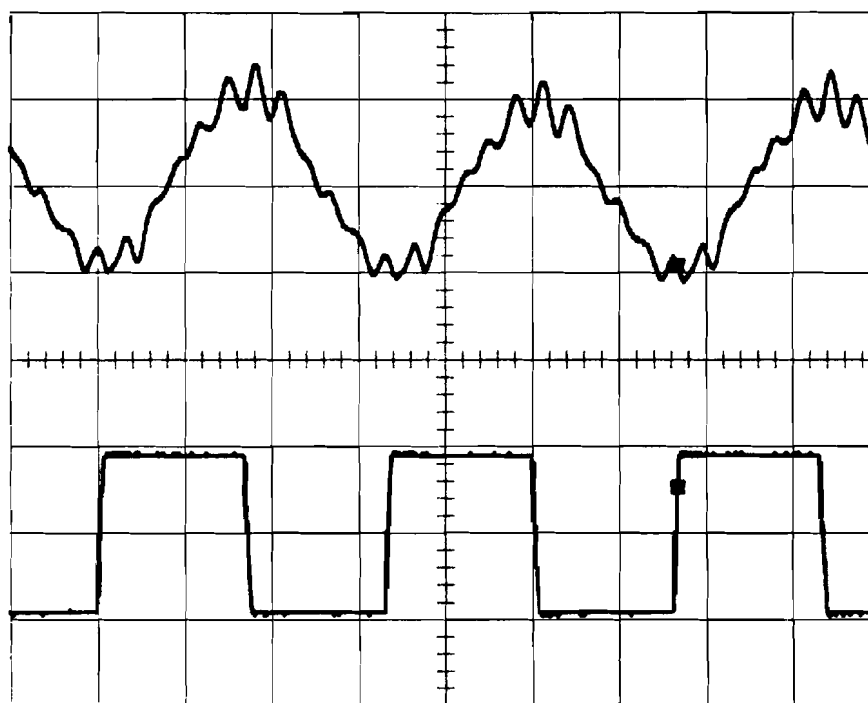


Figure 2.7 Motor and Fan Scroll Assembly Oscilloscope Output for Square Wave Current Input

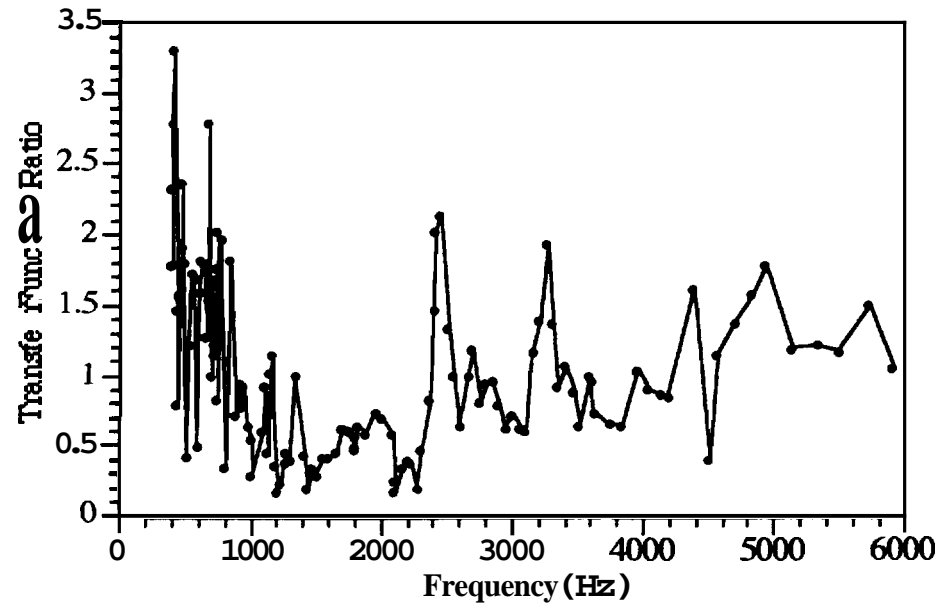


Figure 2.8 Motor and Fan Scroll Assembly Sound to Current Transfer Function

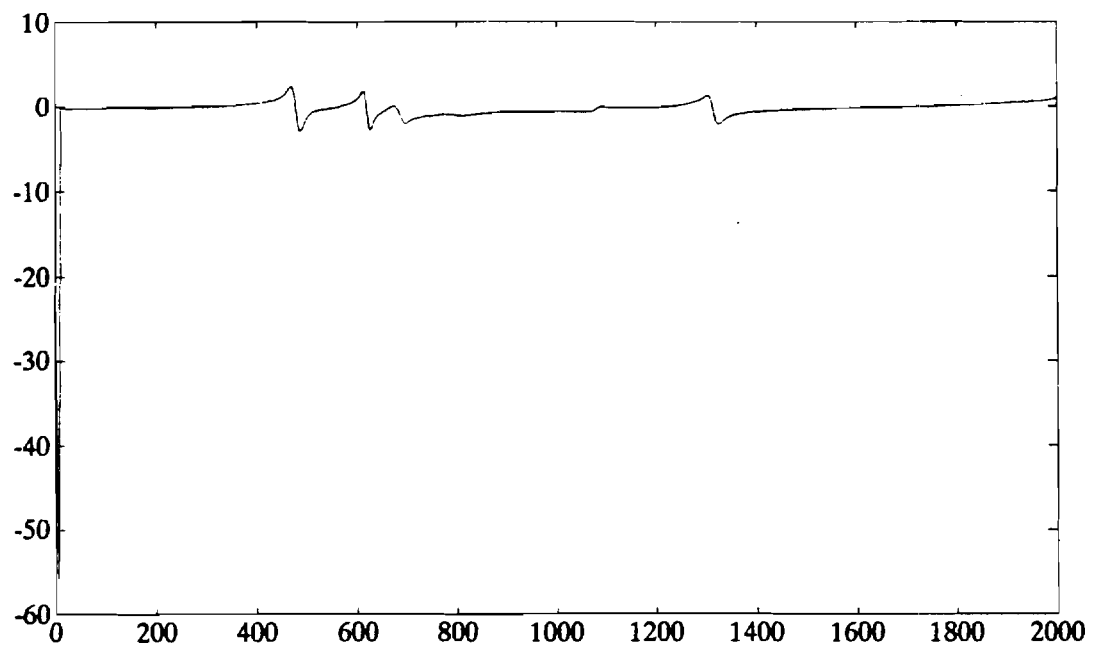


Figure 2.9 Mechanical Transfer Function for Motor Showing 500 Hz and 700 Hz Peaks

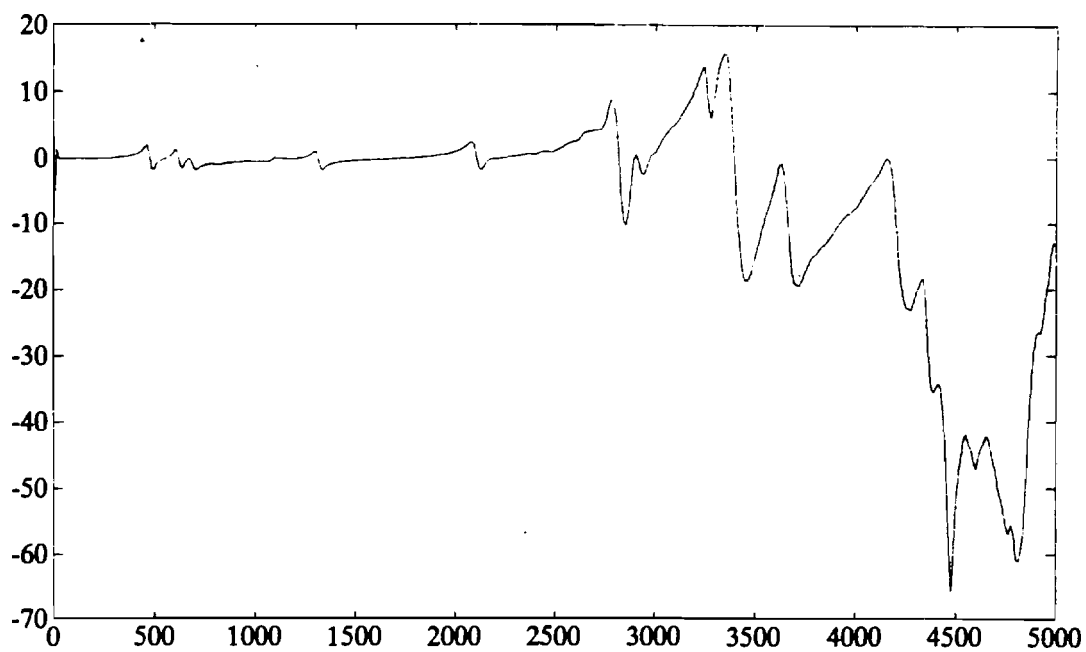


Figure 2.10 Mechanical Transfer Function for Motor Showing 3200 Hz and 4900 Hz Peaks

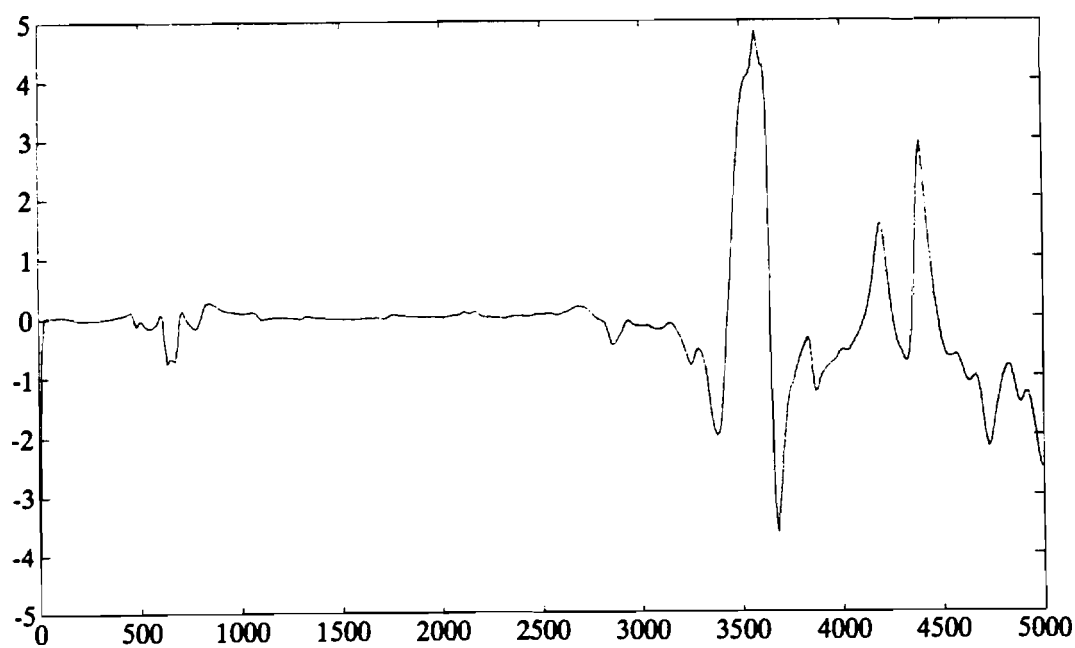


Figure 2.11 Mechanical Transfer Function for Motor Showing 700 Hz and 3200 Hz Peaks

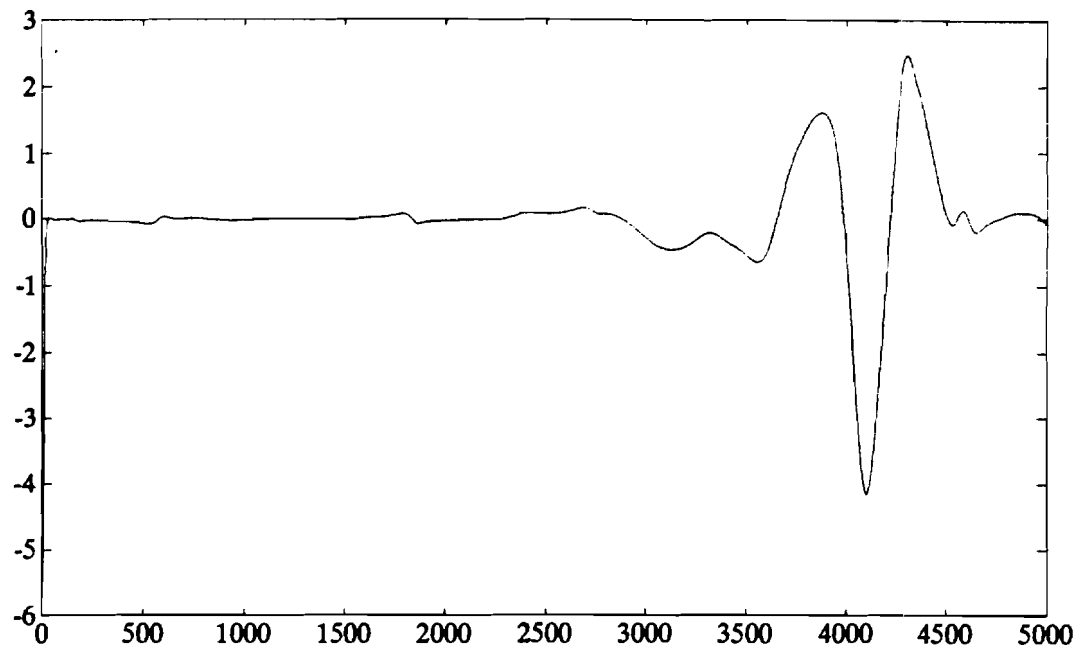


Figure 2.12 Mechanical Transfer Function for Motor and Fan Scroll Assembly Showing 4400 Hz Peak

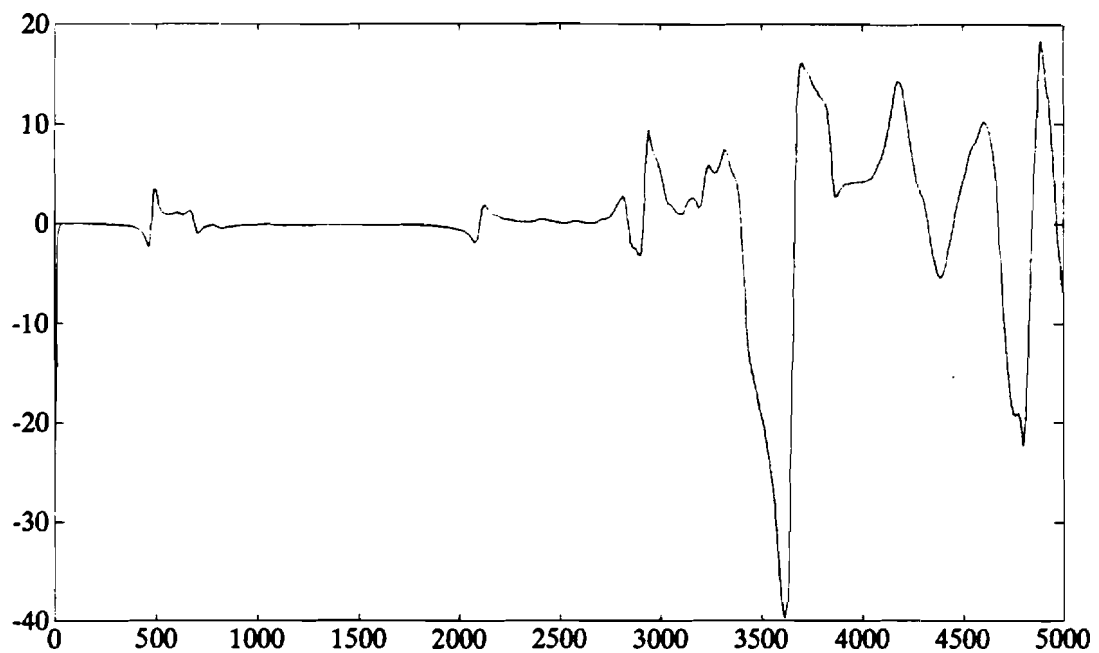


Figure 2.13 Mechanical Transfer Function for Motor Showing 2490 Hz and 4900 Hz Peaks

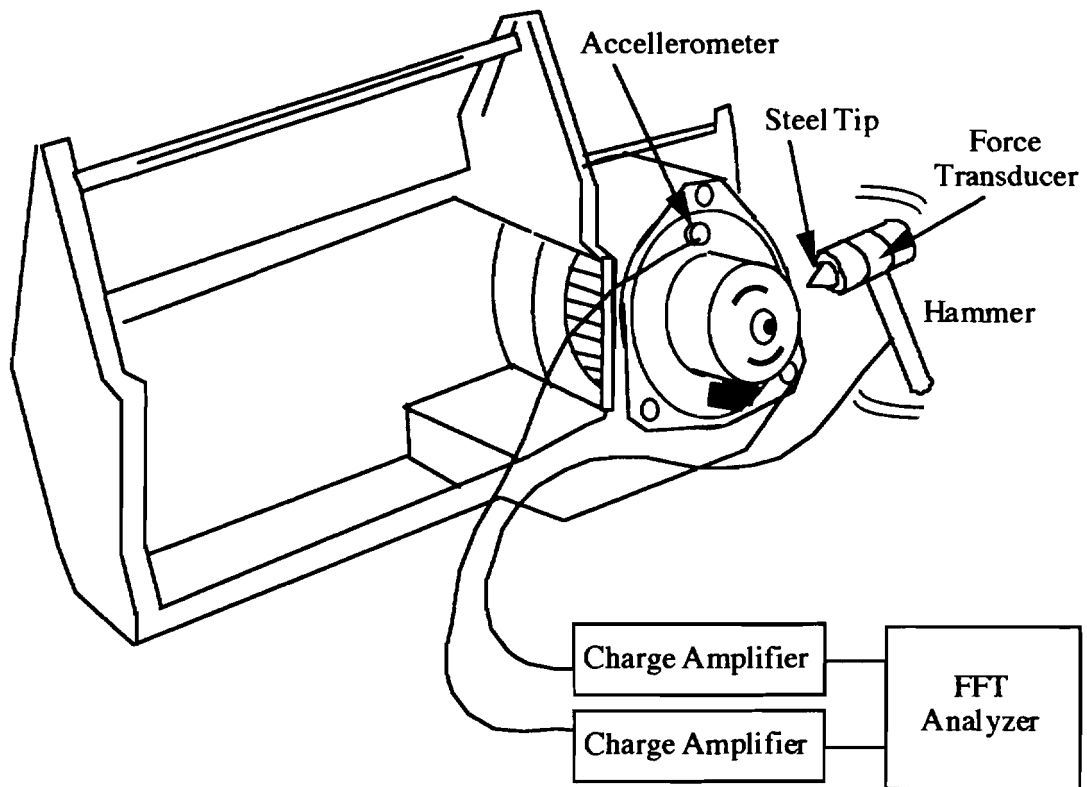


Figure 2.14 Mechanical Transfer Function Experimental Apparatus

CHAPTER 3. INDUCTIVE COUPLING OF ARMATURE COILS IN PERMANENT MAGNET DC MOTORS

The mutual coupling of the armature coils is important to the amount of noise produced by a motor, because the harmonics from the commutating coil's currents are transferred to the other coils through mutual coupling, resulting in electromagnetic forces with the same harmonics. In general the more harmonics in the coil current, the more noise the motor produces due to excitation of the various structural modes.

Individual Coil Self Inductance

There are two factors influencing the coil self inductance: the radius at which the coil is wound and the amount of saturation in the coil's magnetic flux path. With the magnets present in the case, the self inductance of each of the twelve armature coils for a small four pole DC motor are plotted as a function of coil position in Figure 3.1. To obtain the self inductance measurements, the motor end flange was removed to expose the armature positioned within the case and magnet assembly. The leads to the armature coils were cut from the commutator to permit measurements of each coil. Twenty-four inductance measurements per coil taken at 120 Hz were recorded at 15° intervals of armature rotation. Zero degrees was defined as the point where a coil would be centered on one of the magnets in the motor case.

Inductance varies from coil to coil because of winding layering inherent to the manufacturing process. Averaging all the self inductance measurements of Figure 3.1 for each coil, as shown in Figure 3.2, illustrates the difference in self inductance produced by layering. Automatic winders use 2 flyers or leads starting from opposite sides of the armature so that the pattern of winding is repeated once. Coil layering causes differences in the self inductance averages due to the differences in the size of the coils. Smaller coils located at the bottom of the armature slots have a higher self inductance because of greater slot leakage flux. The narrower width at the bottom of the armature slots allows more leakage flux for coils located at these points. Additionally,

the turns of the coils located at the bottom of the slot are more tightly coupled to each other since they are wound around a smaller radius. The coils located at the larger radii have less slot leakage flux because the slots are wider at the periphery of the armature and the larger area which they occupy reduces the portion of the flux which links all the turns of the coil.

Magnets cause saturation in the armature along the path between the magnets. Saturation is related to the slope of the B-H curve. B is the magnetic flux density and H is the field strength as shown in Figure 3.3. In a material such as the steel armature, as the field strength is increased, the magnetic domains align and increase the magnetic flux density in approximately a linear manner. When there are less domains to align, an increase in the field strength no longer increases the magnetic flux density as much as it had before and saturation occurs. Total saturation occurs when the slope of the B-H curve approaches the permeability of air, μ_0 .

Figure 3.1 shows the how the self inductance of the coil varies **with** the position of the coil relative to the permanent magnets. Flux path saturation due to the magnets causes the periodic peaks at 0° , 90° , 180° , and 270° locations of the coil where the coil sides are located between the magnets. Thus self inductance of the coils is dependent on saturation in the coil's magnetic flux path. Lower saturation in a coil's magnetic flux path contributes to a higher self inductance of the coil.

Mutual Inductance Between Individual Coils

The current in the commutating circuits has an effect on the noncommutating current paths because of the mutual coupling between individual coils. An ideal closed form solution was developed into a computer program and its results compared to the experimental data. Differences in the experimental and theoretical data could be attributed to armature saturation which is impossible to account for in the calculations. The mutual inductance between individual armature coils are combined to determine the effective coupling between commutating and noncommutating portions of the armature in the next section.

Ideal Mutual Coil Coupling

In 1929, Hague published closed form solutions for fields in electric motors, many pertinent to permanent magnet DC motors [45]. As one exercise (page 255256) he

developed equations for the field due to a conductor buried in the rotor of an electrical machine with a uniform air gap and infinite stack length. By summing the contributions to the field from two of these conductors located at the coil edges, the field from a single armature coil can be approximated and numerically determined. For this analysis, the magnets are assumed to have the same permeability as air. Dimensions used in the calculations are given in Figure 3.4. Because of the instability of the calculations for radius dimensions greater than 1.0, the radii used in the program are **normalized** to the radius of the outside of the case, g .

The analysis is extended to compute the flux linking a secondary coil located at various angles relative to a primary coil which provides the excitation for the system. Calculations utilize the dimensions of the machine described in Figure 3.4, and the permeability of the various regions also specified in Figure 3.4. The centerline and angular location of the coil edges is determined by the approximate centroid of the coil side bundle. All angular measurements are referenced to the center of the primary coil.

Finding the flux linkage of a secondary coil due to the excitation of a primary coil is the objective of the calculations. Flux linkage per-unit length can be computed by **integrating** the radial component of flux density B_r through the area inside the coil:

$$\lambda = N\Phi = N \int_{\theta_0-\alpha}^{\theta_0+\alpha} r B_r d\theta. \quad (3.1)$$

The flux density's radial component can be expressed in terms of the radial component of the field intensity and by the material permeability in the rotor, μ_3 . The radial component of the field intensity, in turn, is computed from the potential Ω given by Hague:

$$B_r = \mu_3 H_r = \mu_3 \left(-\frac{\partial \Omega}{\partial r} \right) \quad (3.2)$$

Substituting in Equation 3.2 with the potential Ω given by Hague, results in

$$B_r = -\mu_3 \left[\frac{\partial}{\partial r} \left(2i\phi_1 + \sum_{n=1}^m R_{Rn} r^n \sin n \left(\theta - \frac{\beta}{2} \right) - 2i\phi_2 - \sum_{n=1}^{\infty} R_{Rn} r^n \sin n \left(\theta + \frac{\beta}{2} \right) \right) \right]. \quad (3.3)$$

The derivative of the potential Ω results from first taking the derivative of the first and third **terms** in Equation 3.3 at the coil radius $r=c$ where (by Hague p. 216),

$$\frac{\partial \phi_1}{\partial r} = \frac{\partial \phi_2}{\partial r} = 0. \quad (3.4)$$

Then taking the derivative of the second and fourth **terms** of the potential function Ω ,

$$B_r = -\mu_3 \left[\sum_{n=1}^{\infty} R_{rn} n r^{n-1} \sin n \left(\theta - \frac{\beta}{2} \right) - \sum_{n=1}^{\infty} R_{rn} n r^{n-1} \sin n \left(\theta + \frac{\beta}{2} \right) \right]. \quad (3.5)$$

Flux linkage per-unit length can then be computed by integrating the radial **component** of flux density B_r through the area inside the coil:

$$\lambda = -N\mu_3 \left\{ \sum_{n=1}^{\infty} R_{rn} c^n \left[\begin{array}{l} \cos n \left(\theta_0 + \alpha_2 + \frac{\beta}{2} \right) + \cos n \left(\theta_0 - \alpha_2 - \frac{\beta}{2} \right) \\ - \cos n \left(\theta_0 - \alpha_2 + \frac{\beta}{2} \right) - \cos n \left(\theta_0 + \alpha_2 - \frac{\beta}{2} \right) \end{array} \right] \right\}. \quad (3.6)$$

The flux linkage per unit length is multiplied by the stack length to arrive at the flux **linking** the primary and the secondary coil. This flux linkage is scaled by the amount of the self inductance calculated for the primary coil. So the calculated self inductance of the coil shows up as 1.0. Calculated mutual inductance value ratios are shown in **Figure 3.5**.

The shape of the calculated mutual inductance ratio curve is explained by the flux distribution of an energized coil shown in Figure 3.6. Flux from the primary coil is distributed throughout the armature, the three teeth encircled by the energized coil in the **armature** have positive amounts of flux traveling through them as shown by the arrows in Figure 3.6. If there were **1800** lines of flux, each tooth would have approximately **600** lines of flux flowing through it in the positive direction. Teeth on the outside of the coil would have negative amounts of flux passing through them. For explanation purposes, approximate the flux through the outside of the coil at a negative 200 lines per tooth. All of the **1800** flux lines emanating from the primary coil pass through the primary coil in the positive direction, therefore its ratio is 1.0. If the secondary coil were aligned with the primary, as in Figure **3.6a**, nearly all the flux lines from the primary coil would couple the secondary. However, there are no coils wound concentrically in this manner.

With the secondary offset by one tooth from the primary, as shown in Figure 3.6b, a smaller number of flux lines link the adjoining secondary coil, **1000** in the positive direction making the ratio of mutual inductance to self inductance a smaller but still positive ratio of **1000/1800**. The next secondary coil has almost zero net flux of 200 lines for a ratio of **200/1800**. A positive mutual inductance ratio means that the voltage induced in the secondary coil is of the same polarity as that induced in the primary coil. A negative mutual inductance ratio indicates that the net flux through and resulting current in the secondary coil travels in the opposite direction as that of the primary coil. Secondary coils at almost right angles to the primary coil have almost zero net flux. If the coil was at a right angle, the mutual coupling between the coils would be zero. Other coils on the armature have a negative net flux.

Experimentally Obtained Mutual Coupling

There were three different experiments **carried** out: inductance values were obtained for the coils in the case without the magnets, for the coils in the case with the magnets present and magnetized. To obtain the inductance measurements, the motor end flange was removed to expose the armature positioned within the case and magnet assembly. Leads to the armature coils were cut and tinned to permit measurements of each coil. Coils were energized with a variac operating at 60 Hz and **250 mV \pm 5 mV** while multimeters measured the voltage on the primary and secondary coils. Coil self inductance was measured with an inductance meter at 120 Hz. Voltage and coil self inductance were utilized to determine the individual coil inductance.

Coil voltage results from minute resistance drop of the coil added to the time derivative of the coil's flux linkage:

$$V = ri + p\lambda \quad (3.7)$$

For the primary coil, coil 1, that is expressed as:

$$V_1 = r_1 i_1 + p(L_{11} i_1 + L_{12} i_2). \quad (3.8)$$

Flux affecting coil 1 due to coil 1 is $L_{11} i_1$. L_{11} is called the self inductance of coil 1 or the magnetizing inductance of coil 1 plus the leakage inductance of coil 1, i_1 is the current in the primary coil, L_{12} is the mutual inductance between coil 1 and coil 2, the

secondary coil. Flux in the primary coil due to the secondary coil is L_{12} multiplied by the current in the secondary coil. Likewise, for a secondary coil, say coil 2:

$$V_2 = r_2 i_2 + p(L_{22} i_2 + L_{21} i_1). \quad (3.9)$$

Since the secondary coil is open-circuited, i_2 is zero, so the only voltage induced in the secondary is due to mutual coupling. Coil resistance in the primary is so low, **130 mΩ** to **143 mΩ** at **120 Hz**, that the resistive drop can be ignored in equations **3.8** and **3.9**. Dividing Equation **3.8** by Equation **3.9** with these considerations results in Equation **3.10**.

$$\frac{V_1}{V_2} \approx \frac{L_{11} p i_1}{L_{21} p i_1} = \frac{L_{11}}{L_{21}}. \quad (3.10)$$

Thus, the mutual coupling can be found using the voltage ratio and the self inductance of the primary coil:

$$L_{21} = L_{11} \left(\frac{V_2}{V_1} \right). \quad (3.11)$$

This relationship was the basis of the empirically determined mutual inductance values, where V_1 , V_2 , and L_{11} were measured as mentioned.

A comparison of the calculated mutual inductance versus the measured mutual inductance for the motor case without magnets is shown in Figure **3.7**. Calculated values were multiplied by the average measured self inductance for a coil. Some of the difference in the values between the measured and predicted inductance is due to the variation in coil radius due to layering, which is not compensated for in the prediction. Program calculations for the average coil radius and angular position were made based on the centroid for a coil wound so that it fills one half of the armature slot.

Equivalent Inductance of Coil Assemblage

Using connection matrices to produce a simpler two terminal equivalent representation, data from the four pole DC permanent magnet motor was transformed to

a simpler two terminal equivalent form instead of the four terminal form. Connection matrices similar to those used in circuit analysis were utilized.

Use of Connection Matrices

Connection matrices are used in circuit problems, particularly those of the utility industry to provide automatic formulation of **Kirchoff** equations for a circuit. The connection matrices applied here allowed the four terminal DC permanent magnet motor to be viewed as a two terminal DC permanent magnet motor.

The coils and commutator bars are numbered by the position of their centerline in the motor case. The position where the number 1 coil is aligned with the center of one of the magnets is defined as zero degrees of armature displacement. The relative positions of the brushes, commutator bars and coils to the centerline of one of the magnets is shown in Figure 3.8. The brushes are shifted by an angle β while the position of the armature is found by the angle Θ_c between coil 1 and the magnet centerline.

Figures 3.9a and 3.9b are schematics of the commutator bar arrangement showing the connecting coils and the negative and positive brushes. Due to the wave winding of the four-pole motor, its coils do not connect adjacent commutator bars. Vertical arrows with a plus sign below them show the two positive brush positions; likewise vertical arrows with a negative sign below them indicate the negative brush position. Armature current direction is indicated by the horizontal arrows. The angles of each of the 12 commutator bars and armature coils for Θ_c equal to zero are given in Table 1.

Each row in the connection matrix corresponds to a loop between a positive and negative brush or a circuit of one coil when the coil is being shorted by a brush. Each column of the matrix corresponds to a coil of the armature winding. If the current between the brushes travels through the coils in the same direction as the assigned positive current convention (left to right in Figure 3.9), that current is considered positive and the corresponding entry in the connection matrix is a 1. Positive flow of current means that the current is flowing in the assumed positive direction. If the coil is not involved in the circuit between the two brushes, a zero is entered in the connection matrix column corresponding to that coil's number for the row in question. Negative flow of current means that the current is flowing in the assumed negative direction and a negative one is entered in the matrix. With four brushes and no short circuits, there will be four loops formed by segments of the armature wave winding and some external circuit elements. Hence there will be four rows in the connection matrix.

Table 3.1 Relative Location of Armature Bars and Coils

(a) Commutator Bars

Commutator Bar Number	Angular Position
1	345°
2	15°
3	45°
4	75°
5	105°
6	135°
7	165°
8	195°
9	225°
10	255°
11	285°
12	315°

(b) Armature Coils

Coil Number	Angular Position
1	0°
2	30°
3	60°
4	90°
5	120°
6	150°
7	180°
8	210°
9	240°
10	270°
11	300°
12	330°

Equation 3.12 shows the connection matrix corresponding to this brush arrangement shown in Figure 3.9a. The first row of Equation 3.12 corresponds to current flowing between the brushes located at bars 1 and 10, the second row between bars 7 and 10, the third row relates the current flowing between bars 7 and 4 and the final row represents the current flowing between bars 1 and 4.

$$\begin{array}{c}
 \text{Coils} \xrightarrow{\hspace{10em}} \\
 \begin{array}{c}
 1 \dots\dots\dots 12 \\
 \left. \begin{array}{l} 1 \\ 2 \\ 3 \\ 4 \end{array} \right\} \text{Loop} \left[\begin{array}{cccccccccccc}
 0 & 0 & 0 & 1 & 0 & 1 & 0 & 0 & 0 & 0 & 1 & 0 \\
 -1 & 0 & -1 & 0 & 0 & 0 & 0 & -1 & 0 & 0 & 0 & 0 \\
 0 & 0 & 0 & 0 & 1 & 0 & 0 & 0 & 0 & 1 & 0 & 1 \\
 0 & -1 & 0 & 0 & 0 & 0 & -1 & 0 & -1 & 0 & 0 & 0
 \end{array} \right]
 \end{array}
 \end{array} \quad (3.12)$$

Figure 3.9b corresponds to the connection matrix of Equation 3.13:

$$\begin{bmatrix} 0 & 0 & 0 & 0 & 0 & 1 & 0 & 0 & 0 & 0 & 1 & 0 \\ 0 & 0 & -1 & 0 & 0 & 0 & 0 & -1 & 0 & 0 & 0 & 0 \\ 0 & 0 & 0 & 0 & 1 & 0 & 0 & 0 & 0 & 0 & 0 & 1 \\ 0 & -1 & 0 & 0 & 0 & 0 & 0 & 0 & -1 & 0 & 0 & 0 \\ 0 & 0 & 0 & 1 & 0 & 0 & 0 & 0 & 0 & 0 & 0 & 0 \\ -1 & 0 & 0 & 0 & 0 & 0 & 0 & 0 & 0 & 0 & 0 & 0 \\ 0 & 0 & 0 & 0 & 0 & 0 & 0 & 0 & 0 & 1 & 0 & 0 \\ 0 & 0 & 0 & 0 & 0 & 0 & -1 & 0 & 0 & 0 & 0 & 0 \end{bmatrix} \quad (3.13)$$

The first four rows of the connection matrix represent the noncommutating circuits in Figure 3.9b. Rows 1 through 4 of the connection matrix depict the similar circuits formed between the positive and negative brushes as shown in Figure 3.9a and Equation 3.12 except for the removal of four commutating coils. Row 5 corresponds to the coil being shorted by the two positive brushes causing a short between commutator bars 1 and 8. It is assumed that the voltage drop between both brushes of similar polarity is negligible. The matrix entry for the coil current in row 5 is chosen as positive, because before it was shorted, it was in a circuit where the current was flowing in a positive direction.

Connection matrices allow the calculation of the loop inductance for the circuits in the motor from the self and mutual inductance data for each coil. A connection matrix pre multiplies and post multiplies the inductance matrix to accomplish this:

$$L_{reduced} = CLC^T \quad (3.14)$$

Thus, the inductance matrix can be reduced from a 12 by 12 matrix to a 4 by 4 matrix for the noncommutating case. Diagonal entries in the matrix represent the equivalent self inductance of each coil to itself. Off diagonal entries in the matrix correspond to equivalent mutual inductance between circuit paths. Since the winding was produced by two flyers winding the armature, the resulting reduced inductance matrices should have two groups of similarly valued rows. Variation between the two groups of values should not be great. In the commutating case, where four coils are being shorted, the resulting reduced induction matrix is a 8 by 8 because there are eight separate circuits in the motor. Reduced inductance matrix entries represent the mutual and self inductance values as they did in the noncommutating case.

To further simplify the analysis, the currents in parallel paths are assumed to be equal. In this case, all the currents in the noncommutating coils are equal to i_a . The induced voltages in the non-shorted coil paths should all be the same since the brushes are symmetrically located. Each parallel path should have identical resistance, inductance and induced voltage. The actual parameters of each path differ by a small amount due to the layering of the winding and manufacturing variations which lead to slight asymmetry. These differences will be ignored for this study. Thus, Thus in the noncommutating case, writing the inductance voltages of each of the paths as v_a ,

$$\begin{bmatrix} V_a \\ \cdot \\ \cdot \\ V_a \end{bmatrix} = \begin{bmatrix} L_{11} & \cdot & \cdot & L_{14} \\ \cdot & \cdot & & \\ \cdot & & \cdot & \\ L_{41} & & & L_{44} \end{bmatrix} \begin{bmatrix} i_a \\ i_a \\ i_a \\ i_a \end{bmatrix} \quad (3.15)$$

and assuming $L_{11} = L_{22} = \dots = L_{44}$ and off diagonal terms are similarly equal, then equivalent inductance in the a coil path is found by summing the inductance in each row and averaging all the rows in the matrix. v_a is then equal to,

$$v_a = \sum_{X=1}^4 \frac{(L_{X1} + L_{X2} + L_{X3} + L_{X4})}{4} i_a. \quad (3.16)$$

For commutating positions, current in the noncommutating paths is i_a as above and similarly all the short circuit currents are assumed to be equal by symmetry to i_b , current through the “b” coils. This simplification allows the motor to be analyzed as if it has two coils. The nonshorted coils connected between the brushes will be referred to as the “a” circuit. while the shorted coils will be the “b” circuit.

Calculation of Equivalent Inductance Values

Connection matrices were utilized to arrive at reduced equivalent inductance matrices. The reduced equivalent matrices were examined to determine if there should be any coupling between the commutating and noncommutating coils in the ideal case where the magnet permeability is the same as air and the iron has linear properties. This was accomplished using the inductance ratios calculated from the program based on Hague's method. The inductance ratios were given the correct sign convention

according to the positive or negative coupling of the coils. Results of this analysis showed that there should be no coupling between commutating and noncommutating coils because the entries in the reduced equivalent inductance matrices for mutual coupling between them were zero.

Reduction of Experimental Data

A close examination of the experimental data reveals the effects of the winding layers. For example, for the data gathered when the magnets were not present in the case, with brushes positioned at 15° from a commutator slot, the matrix for the **non**-shorted condition is:

$$\begin{Bmatrix} \begin{array}{|c|c|c|c|} \hline 483.76 & 69.04 & 92.30 & 78.25 \\ \hline 77.86 & 535.98 & 84.26 & 109.24 \\ \hline 92.60 & 79.68 & 482.50 & 68.40 \\ \hline 85.33 & 107.03 & 78.02 & 536.80 \\ \hline \end{array} \end{Bmatrix}. \quad (3.17)$$

It is clearly evident that rows 1 and 3 of Equation 3.17 correspond to each other, being wound first or last in the coil winding pattern, and that rows 2 and 4 also coincide with each other in the coil winding order. Finding the equivalent circuit "a" inductance using data from Equation 3.17 and putting it into Equation 3.16 gives $765.27 \mu\text{H}$ for the equivalent inductance of coil "a."

The empirical data also shows the effects of armature saturation. In Figures 3.10-3.12 the equivalent inductance values taken with the magnets present in the case are lower than those taken when the magnets were not in the case. Armature saturation is evidenced by the drop in self inductance observed when the permanent magnets are placed in the motor. Coil "a" self inductance is shown in Figures 3.10 and 3.12, coil "b" self inductance is shown in Figure 3.11. These data differ from the self inductance of the individual coils shown in Figure 3.1. The difference results from the flux paths produced by individual coils as compared to that resulting from a collection of coils as shown in Figure 3.13. When only one coil is energized with its axis aligned with a magnet, the flux travels in a local region of low saturation as in Figure 3.13a. Thus for the single coil, the inductance is highest when the coil axis is aligned with the magnet. For the resultant circuit, the flux travels through the entire armature as shown in Figure 3.13b. This portion of the armature is much more saturated and results in the lowest

inductance. Thus for the collection of coils the lowest inductance occurs when the magnetic axis of the winding is aligned with the magnets.

Armature saturation resulting from the presence of magnets in the case also causes mutual coupling between the shorted and non shorted coils shown in Figure 3.14. It is easier for the magnetic flux to travel through the unsaturated region between magnets than through the saturated flux path of these magnets. The "a" and "b" circuits should not be linked if the coil flux centerlines are perpendicular to each other, unless something causes skewing of the coil flux paths. If the magnet permeance, which is slightly higher than that of air, causes the distortion of the flux paths then the lines of flux will bend toward the magnet and the coils will be mutually coupled as shown in Figure 3.15. If saturation due to the presence of the magnets causes the coupling between the flux paths, the lines of flux bend away from the magnets and the coils are also mutually coupled as shown in Figure 3.16. Since the effect of each of these conditions is similar, discernment of the actual cause for the coupling is quite difficult until the self inductance variation is considered. Since the self inductance of the non-shorter coil is highest for 0° **brush** shift where the a-coil axis is directed between the magnets, the cause for the inductance variation and for the mutual coupling can be deduced to be saturation effects.

Approximations for the Equivalent Inductance

Figure 3.10 shows the self inductance of coil "a" for the shorted condition, L_{aac} . Using the experimental measurements for the case with magnets, the equivalent reduced self inductance may be approximated by

$$L_{aac} = 463.73 + 39.7 \sin(4\Theta_c + 108.7). \quad (3.18)$$

The armature position relative to the magnet center is Θ_c . Equation 3.18 is a good approximation for this inductance. The squared difference between 5 of the experimentally derived points and the function was less than $10^{-2} \mu\text{H}$. Coil "a" has its lowest self inductance at 26.3° , 116.3° , 206.3° , and 296.3° , when the resultant flux path passes through the steel saturated by the magnets.

The self inductance of coil "b" for the shorted condition, L_{bb} , is shown in Figure 3.11. The corresponding approximation is

$$L_{bb} = 203.4 + 9.8\sin(4\Theta_c - 15.25). \quad (3.19)$$

L_{aa} shown in Figure 3.12 is the self inductance for the "a" circuit during periods when commutation is not occurring. It may be approximated by

$$L_{aa} = 667.09 + 70.25\sin(4\Theta_c + 95.125). \quad (3.20)$$

Similarly, an approximation for L_{ab} , the mutual coupling between nonshorted and shorted circuits is

$$L_{ab} = 30.375\sin(4\Theta_c + 5). \quad (3.21)$$

Figure 3.17 shows the excellent correlation between this approximation for L_{ab} and the experimentally measured values of L_{ab} .

Effect of Inductance Variation and Mutual Coupling on Noise

Saturation of the armature by the permanent magnets causes measurable coupling between the commutating and noncommutating coils. Current ripples in the commutating coils are transferred to the noncommutating coils through mutual coupling. Variations in the self inductance of both commutating and noncommutating coils also produces additional fluctuations in the armature current. Chapter 4 examines the use of different motor models in representing these effects.

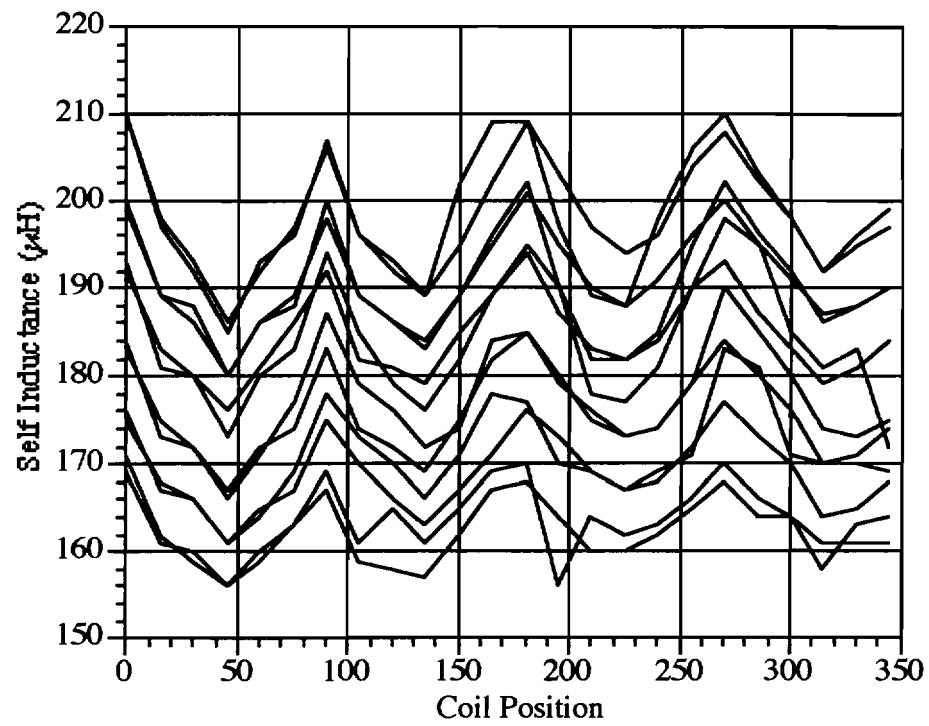


Figure 3.1 Coil Self Inductance Versus Coil Position

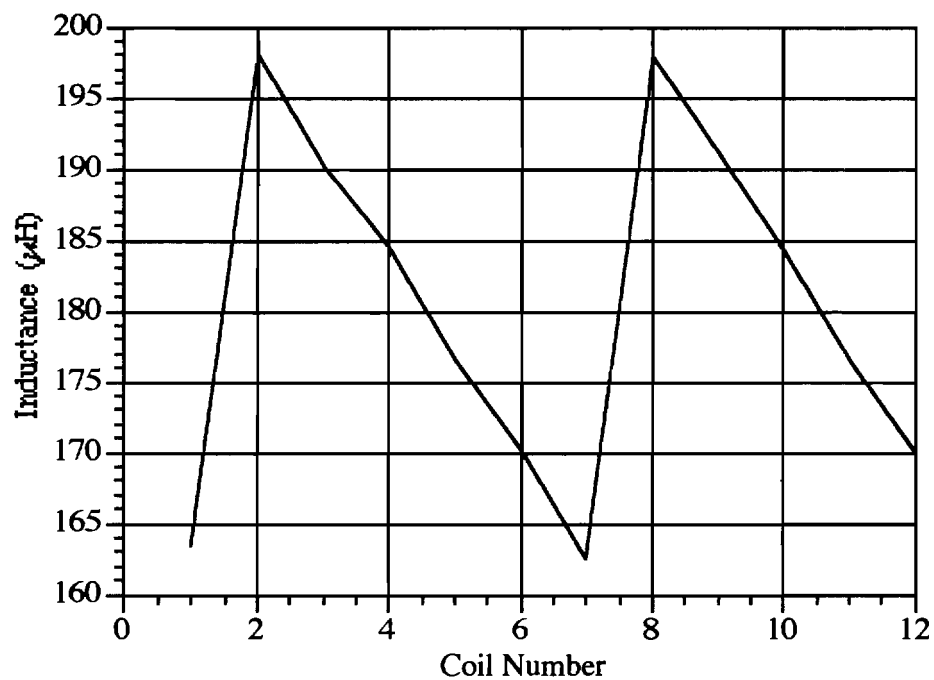


Figure 3.2 Average Coil Self Inductance Versus Coil Number

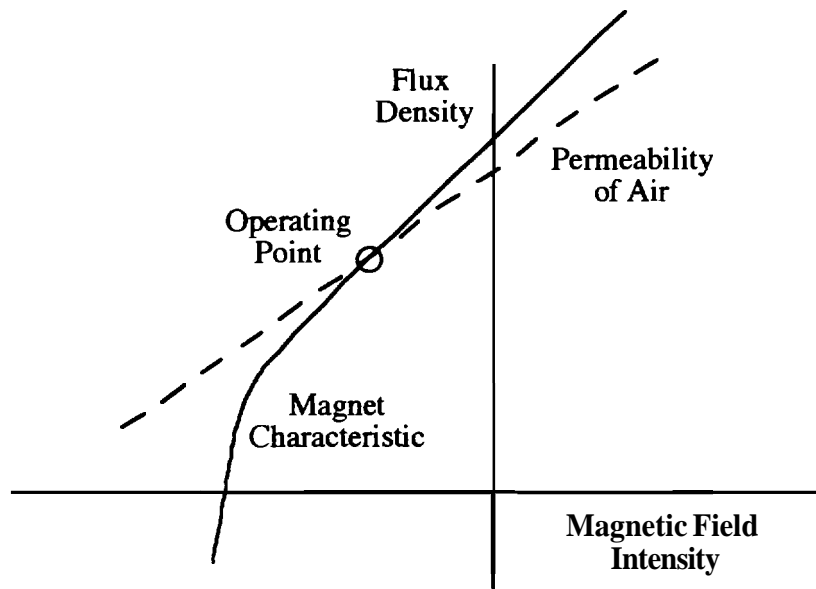


Figure 3.3 B-H Curve for Air and Magnet Material

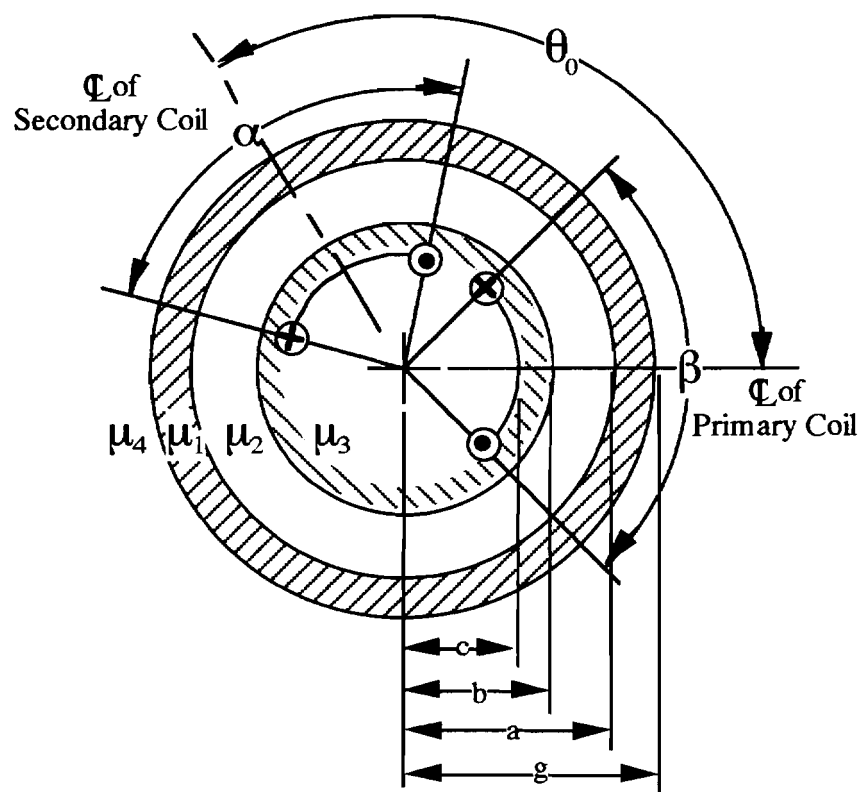


Figure 3.4 Two Coils Embedded in Armature Within Case

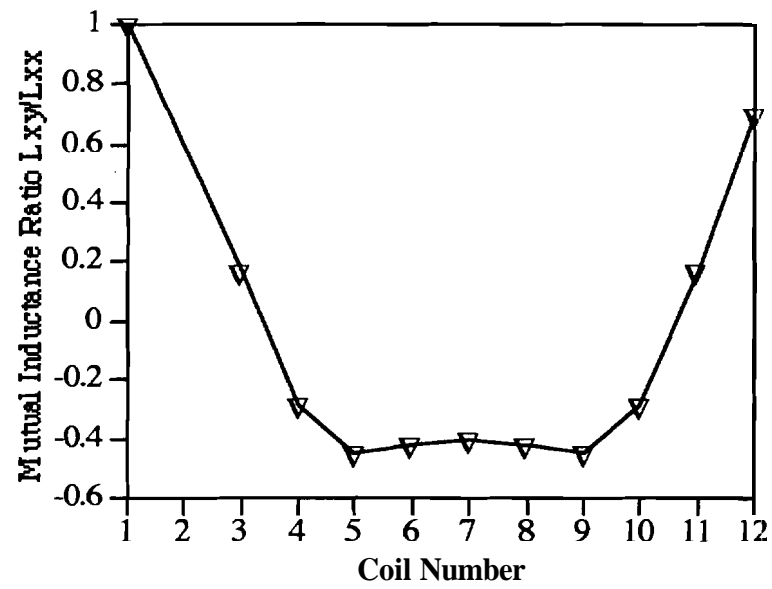


Figure 3.5 Calculated Mutual Inductance

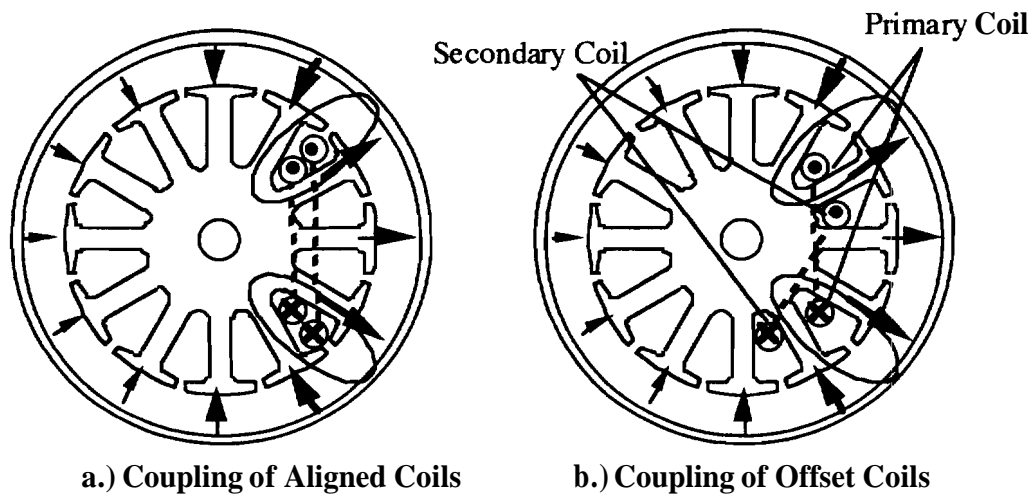


Figure 3.6 Flux Distribution from Primary Coil

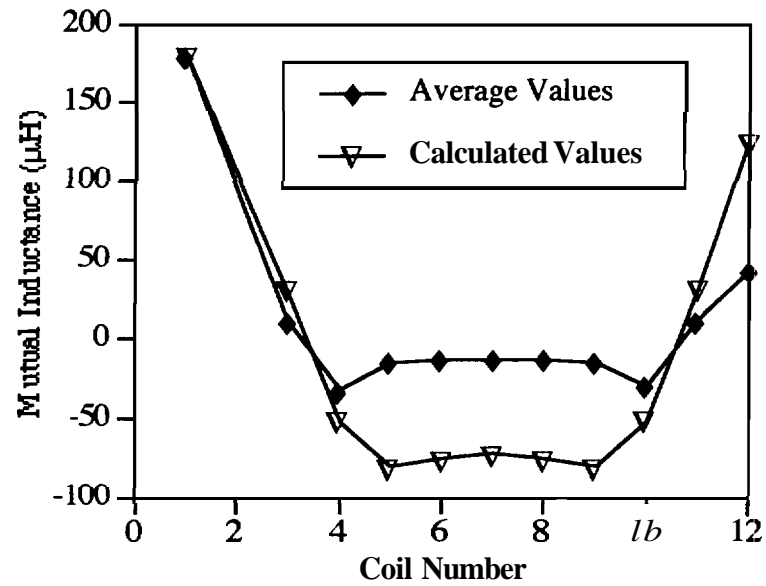


Figure 3.7 Mutual Inductance: Empirical for Case Without Magnets Vs. Calculated

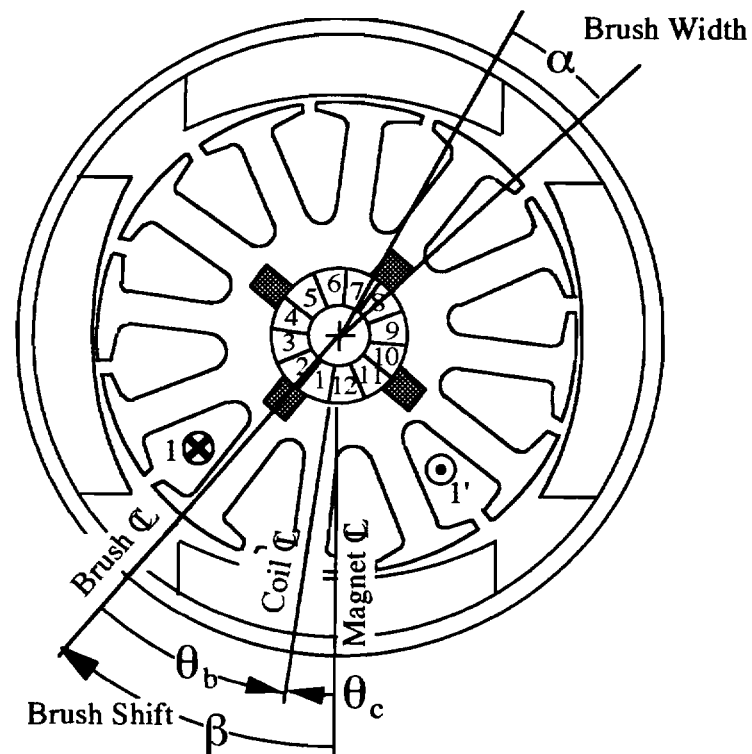
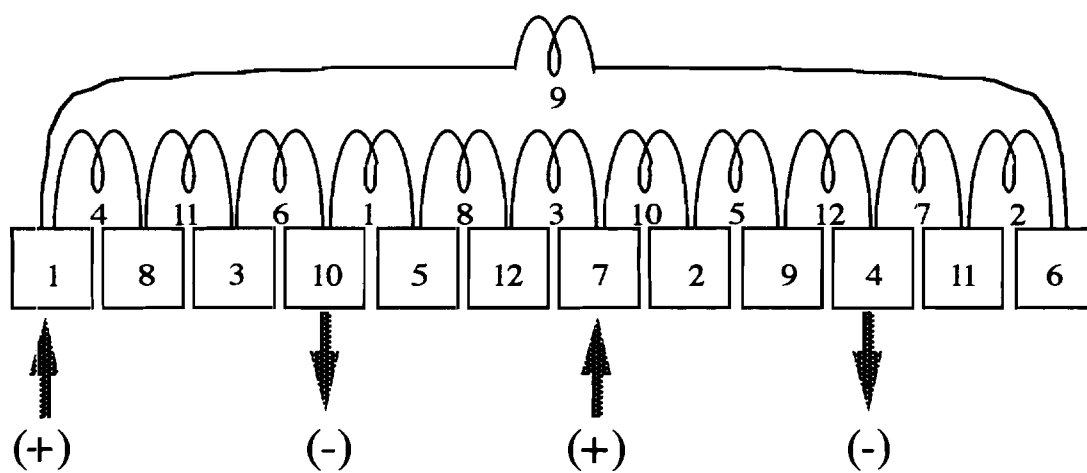
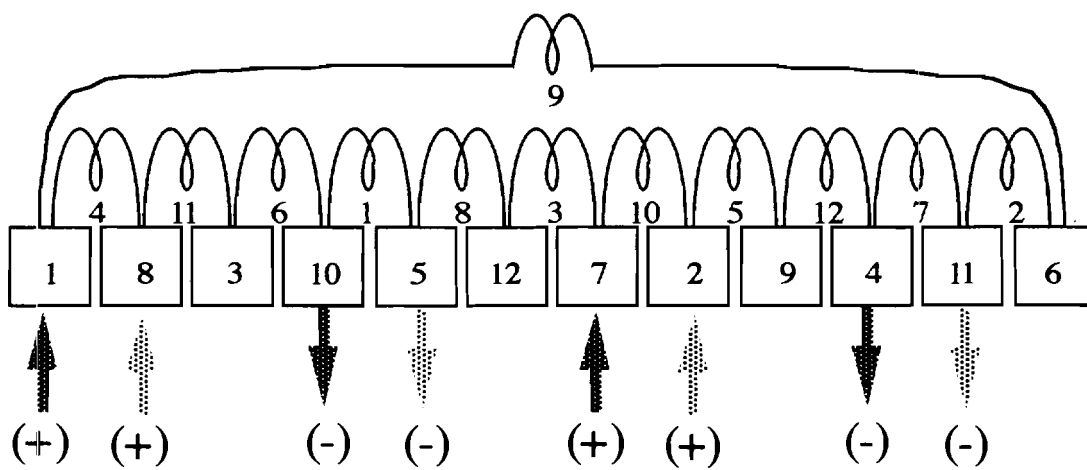


Figure 3.8 Angular Relationship Between Magnets, Brushes, and Commutator



(a) Non-Shorted Condition



(b) Shorted Condition

Figure 3.9 Four Brush Circuit Configurations

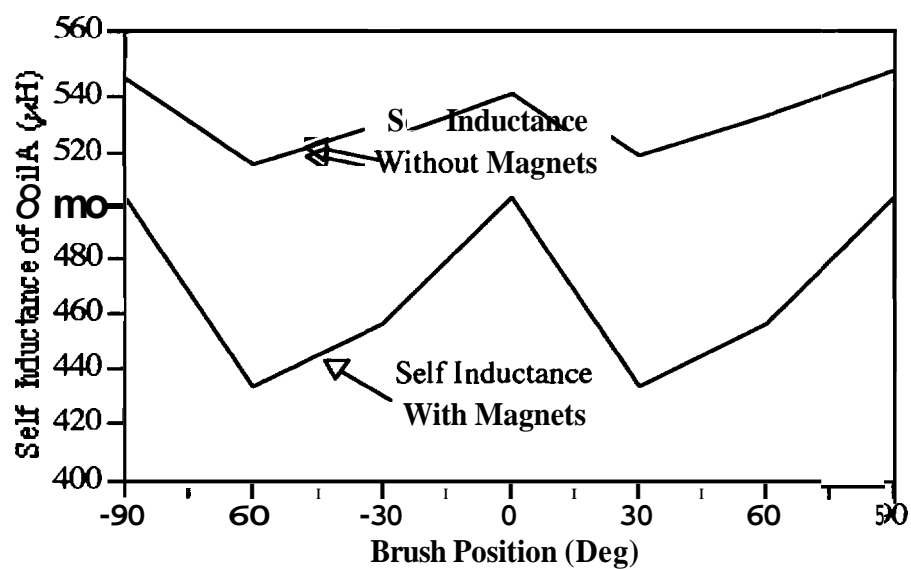


Figure 3.10 Self Inductance of 'a' Coil for Shorted Condition

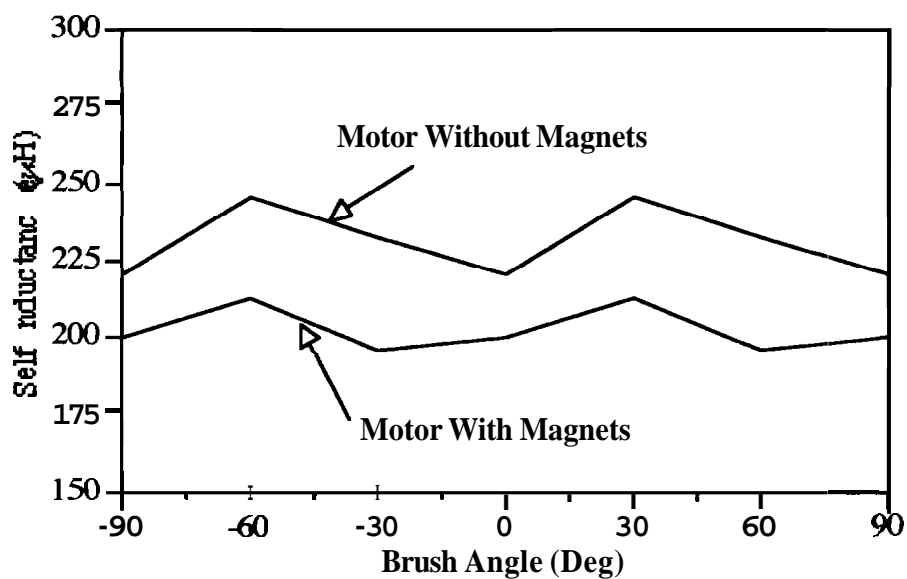


Figure 3.11 Self Inductance of "b" Coil for Shorted Condition

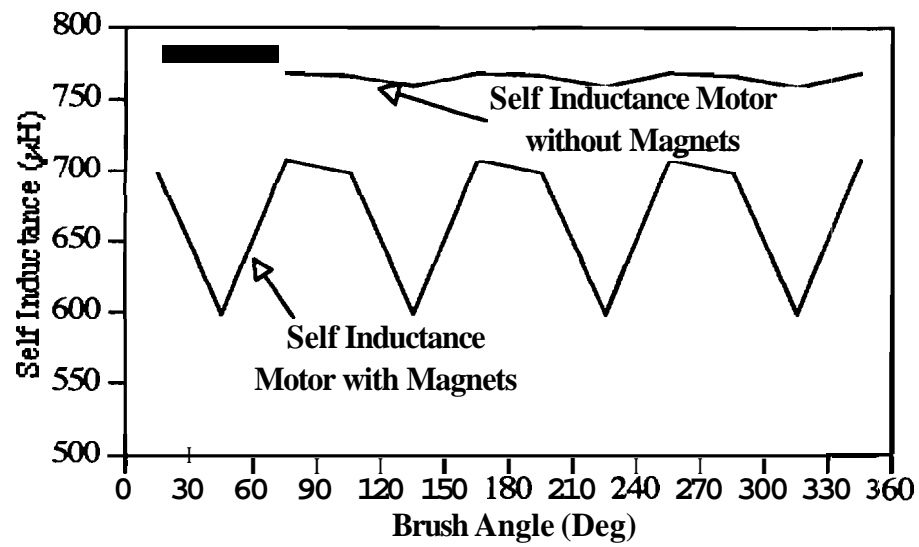


Figure 3.12 Experimental Self Inductance of "a" Coil for Non-Shorted Condition

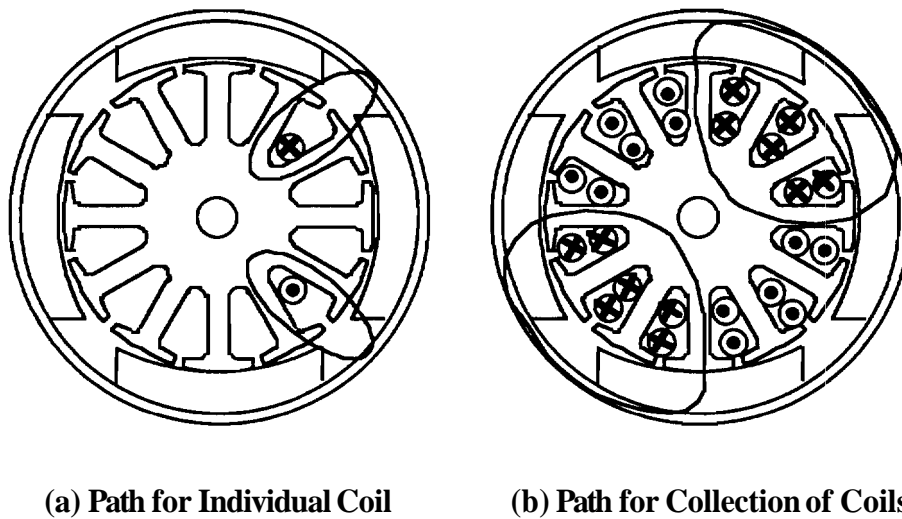


Figure 3.13 Resultant Flux Paths

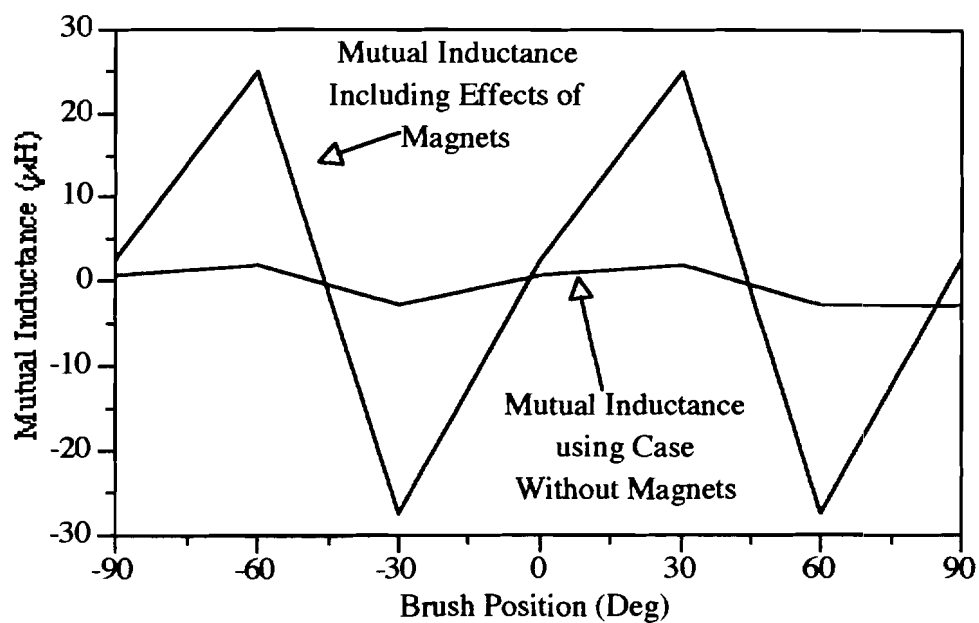


Figure 3.14 Experimental Mutual Inductance of "a" and "b" Coils for Shorted Condition

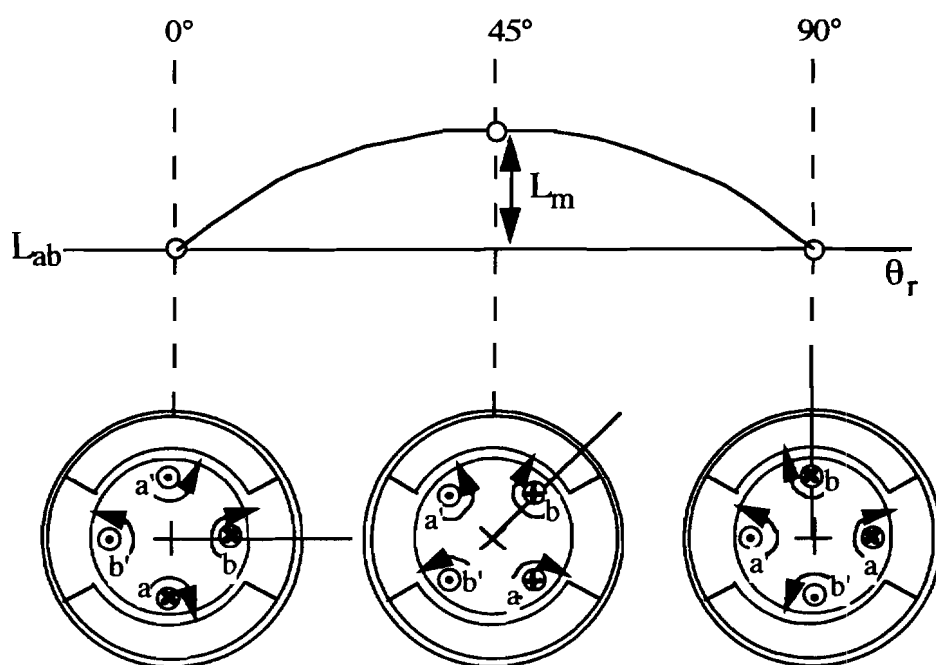


Figure 3.15 Magnet Permeance Effects on Mutual Coupling

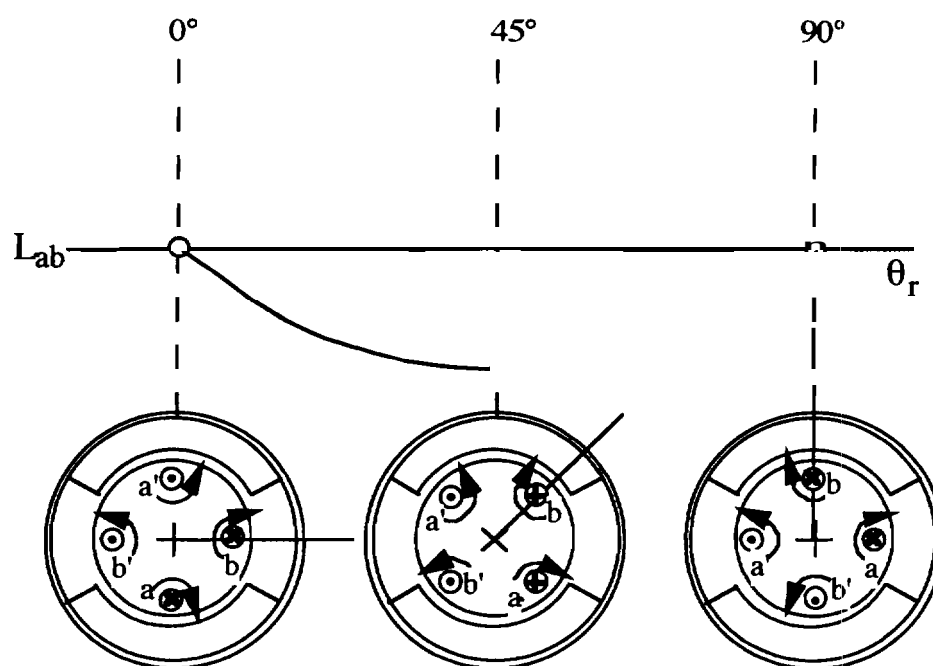


Figure 3.16 Magnet Saturation Effects on Mutual Coupling

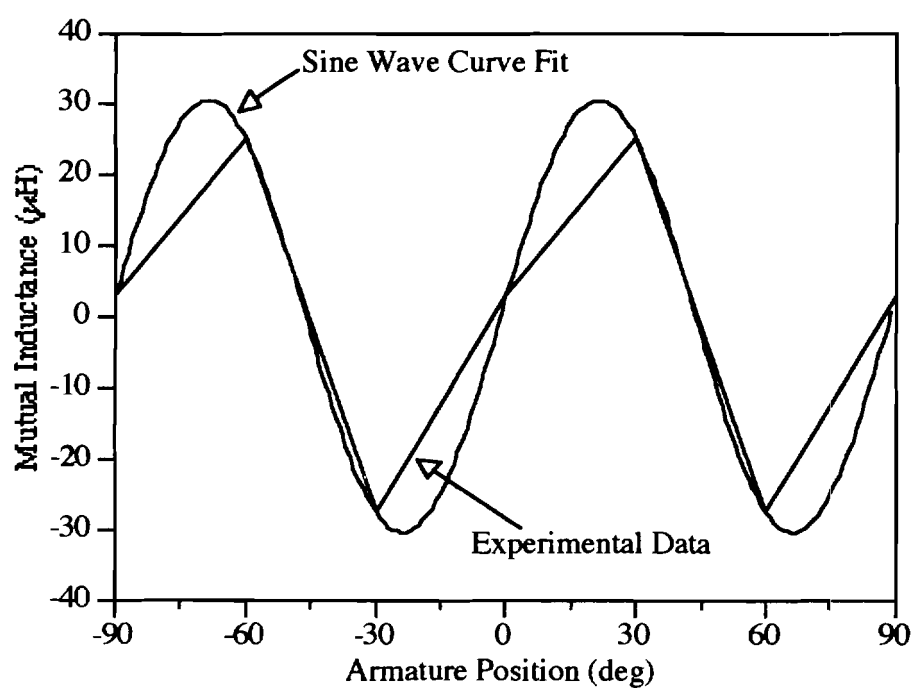


Figure 3.17 Correlation of L_{ab} Equation and Experimental Data

CHAPTER 4. SIMULATION OF LINE CURRENT

As shown in Chapter 2, the line current wave form is related to the **amount** of noise a DC permanent magnet motor produces. Discontinuity of the commutation process impacts the equivalent motor inductance, back voltage, and resistance. **Mutual** coupling between commutating and noncommutating coils and similar brief mutual coupling with the current in the commutation arc result in spikes in the coil current **and** audible noise **from** the motor.

DC Permanent **Magnet** Motor Models

Four motor models will be examined. Their correlation with the experimental current wave form and their primary advantages and disadvantages are discussed. Experimental data described in the last chapter was used in each model. The first three models are examined only briefly because they serve only as introduction to the fourth mutual coupling model.

The first model is the conventional model. It gives information on the general direction of the current and its average value. Secondly, a model with position dependent back voltage which approximates a discontinuous commutation process is discussed. The third model includes position dependent sine wave **approximations** to the inductance as discussed in Chapter 3. The last model contains mutual **coupling** between the shorted, commutating, and noncommutating coils and a representation of the arc struck between the commutation bars and the brushes after the motor has mechanically commutated. This model, which has not been discussed in the literature, is explained here in detail. Each model was numerically simulated using the **fourth** order Runge Kutta integration algorithm.

Preliminary Permanent Magnet Motor Models

Conventional DC motor models represent the major electrical parts of the motor as stationary circuits as shown in Figure 4.1. They do not include the effects of **commutation** current on motor performance or line current. Generally they assume that the values do not change as a result of brush shift or commutation.

Average Value Model

In this conventional model the motor consists of four parallel paths each carrying a current one forth the magnitude of the current seen at the terminals-- that which was experimentally measured. Each path sees the same applied voltage. Within each path is the resistance and inductance of three coils in series and the speed dependent back voltage generated by coils rotating in the magnetic field of the permanent magnet. The equation for the loop is

$$V_{DC} = V_{br} + (r_t + r_a)i_a + p\lambda_a, \quad (4.1)$$

Where 0.5 V was used for V_{br} , the brush drop voltage and 0.12 Ω was used for r_t , the external terminal resistance. The flux linkage for the path is

$$\lambda_a = p(L_{aa}i_a) + \lambda_{ga}, \quad (4.2)$$

λ_{ga} being the flux linkage between the magnets and coils in the path. Its derivative is the speed dependent back voltage, e_{ga} , which here is represented as a linear function of speed. The resulting differential equation used in the Runge Kutta integration is

$$pi_a = 1 / L_{aa} (V_{DC} - V_{br} - (4r_t + r_a)i_a - e_{ga}). \quad (4.3)$$

This model has advantages and disadvantages. It is easy to program and runs quickly. It gives the general idea of current wave form magnitude as **shown** by Figure 4.2. It results in a good approximation of steady state current. However, it is hard to determine the parameter values for the model because of motor build variances such as **brush** shift and variation in the brush width as the brush faces seat on the commutator. It does not give any information on the harmonic content of the current. The resulting

current estimate is lower, but on the same order of magnitude as the **actual** current wave form shown in Figure 4.6.

Time Varying Model

The second model uses Equation 4.3, but accounts for variations in back voltage and resistance due to commutation. Equivalent terminal back emf, e_{ga} , for the noncommutating segment and e_{gac} for the commutating portions of the motor cycle are described as follows:

$$e_{ga} = -2\omega_r n_c \Phi_{\max} \left(\sin 2(\Theta_c + 90^\circ) + \sin 2(\Theta_c + 300^\circ) + \sin 2(\Theta_c + 150^\circ) \right) \quad (4.4)$$

$$e_{gac} = -2\omega_r n_c \Phi_{\max} \left(\sin 2(\Theta_c + 300^\circ) + \sin 2(\Theta_c + 150^\circ) \right) \quad (4.5)$$

Information on the brush position and brush angular width defined in Figure 3.8 tells the program when it should **commutate**. The program keeps track of the relative location of the commutator bar slot and the brush center with Θ_b . Each commutator slot is assumed to be aligned with the centerline of an armature coil. The brushes are shifted an angle β from the center of a magnet. Thus the coil position Θ_c is equal to the sum of β and O_c .

If the distance from the centerline of the brush to the gap between two commutator bars is less than half the brush width, a , the motor is commutating. The location of the **centerline** of a coil relative to the magnet centerline determines the back voltage. Since the commutation cycle is periodic, Θ_c is reset every 30° of rotation. When Θ_c is zero, coil 1 is lined up with the magnet centerline. Circuit resistance values used for the commutating portion of the program are two thirds those used for the **noncommutating** portion of the program to account for the one out of three coils which is removed from each circuit path during commutation. Inductance values used in the **program** are the DC offset values for the commutating and noncommutating coil "a" self inductance described in Chapter 3. Current in the commutating coils is ignored in this version of the program.

A current wave form from the program is shown in Figure 4.5. It is apparent in this graph that the discontinuous nature of the sinusoidal back voltage, resistance and inductance produce a current wave form which resembles an actual current wave form run from a production motor at the same speed, voltage, and brush shift shown in Figure

4.6. A brush width of 21° resulted in the wave form of Figure 4.5. The actual brush width in the motor under test is a function of the amount of wear on the brush face, but **must** be less than 30° **since** the brush is not wider than a single commutator bar.

Time Varying Model with Position Dependent Inductance

The third model uses a position dependent inductance resulting in the differential equation,

$$p i_a = 1/L_a (V_{DC} - V_{br} - (4r_t + r_a + pL_{aa})i_a - e_{ga}). \quad (4.6)$$

The sinusoidal wave form description of the inductance derived from experimental data in Chapter 3 is used in the solution of Equation 4.6. This model is one step more complex than the second model. Its wave form is shown in Figure 4.7. This wave form closely corresponds to the experimental wave form. From this model and the previous version it can be seen that much of the information relating to the current wave form is contained in the discontinuous nature of the equivalent circuit and in the **position** varying inductance and back voltages of the noncommutating current path.

Mutually Coupled Arcing Model

The mutually coupled arcing model is comprised of three time-varying circuits. It contains everything from the third model as well as the mutual coupling between the commutating and noncommutating coils. This coupling has an effect **during** mechanical commutation and when an arc is drawn between the commutator bars after mechanical commutation occurs. The arc is produced between the trailing edge of each brush and the **adjacent** commutator bar.

The noncommutating portion of the motor circuit is modeled using the same circuit previously described in Figure 4.4. During commutation, two currents are produced: the non-shortened path current i_a and the short circuit current i_b as illustrated in Figure 4.8. If commutation and other effects are symmetrical for each of the four parallel winding paths, only one of each shortened and non-shortened path need be modeled. The Kirchhoff voltage loop equations for these paths lead to

$$\begin{bmatrix} V_a \\ V_b \end{bmatrix} = \begin{bmatrix} r_t + r_a & 0 \\ 0 & r_b \end{bmatrix} \begin{bmatrix} i_a \\ i_b \end{bmatrix} + p \begin{bmatrix} \lambda_a \\ \lambda_b \end{bmatrix} \quad (4.7)$$

and

$$p \begin{bmatrix} \lambda_a \\ \lambda_b \end{bmatrix} = p \left\{ \begin{bmatrix} L_{aac} / 4 & L_{ab} \\ L_{ab} / 4 & L_{bb} \end{bmatrix} \begin{bmatrix} i_a \\ i_b \end{bmatrix} + \begin{bmatrix} \lambda_{gac} \\ \lambda_{gb} \end{bmatrix} \right\}. \quad (4.8)$$

The initial value of i_b is $-i_a$, the current in the noncommutating path just prior to the short circuit by the brush. The current in the shorted coil is supposed to reverse during commutation and ideally would change from $-i_a$ to 0. Since the “b” path is short circuited by the brush, V_b is 0.

Two possible arcing circuits are depicted by Figures 4.9 and 4.10. The circuit of Figure 4.9 is the first, most obvious choice for the loop equations but proved to yield unstable results. Figure 4.10 was successfully programmed and proved to integrate with greater reliability. The loop equations from the circuit of Figure 4.10 are given by

$$\begin{bmatrix} V_x \\ V_y \end{bmatrix} = \begin{bmatrix} r_1 + r_2 + 4r_t + r_a & r_1 + 4r_t + r_a \\ r_1 + 4r_t + r_a & 2r_1 + 4r_t + r_a + r_b \end{bmatrix} \begin{bmatrix} i_x \\ i_y \end{bmatrix} + p \begin{bmatrix} \lambda_x \\ \lambda_y \end{bmatrix}, \quad (4.9)$$

where the flux linkages are defined by,

$$p \begin{bmatrix} \lambda_x \\ \lambda_y \end{bmatrix} = \begin{bmatrix} L_{aac} & L_{aac} \\ L_{aac} & L_{aac} + L_{bb} \end{bmatrix} \begin{bmatrix} i_x \\ i_y \end{bmatrix} + \begin{bmatrix} e_{gac} \\ e_{gac} + e_{gb} \end{bmatrix}. \quad (4.10)$$

The loop currents i_x and i_y relate to the i_a and i_b currents by the following transformation:

$$\begin{bmatrix} i_a / 4 \\ i_b \end{bmatrix} = \begin{bmatrix} 1 & 1 \\ 0 & 1 \end{bmatrix} \begin{bmatrix} i_x \\ i_y \end{bmatrix} \quad (4.11)$$

V_x and V_y are both equal to $V_{DC} - V_{br}$.

Since the arc voltage is approximately constant [41,46], r_2 was modeled using a variable resistance. It was calculated by dividing the arc voltage by the current i_b from the previous step. Arcs were considered to be extinguished when i_b reached a value below .05A, even though occasionally an arc can be sustained with a current of .01A [41]. The arc voltage was chosen to 16 V, the average of the 12 V arc expected at the positive brush and the 20 V arc expected at the negative brush [41].

Figure 4.11 is a wave form from the mutually coupled arcing model program that is **very** similar to the actual motor wave form shown in Figure 4.6. The correlation **between** empirical and predicted wave forms points out the robust nature of the model. The model's parameters were taken from various production motors. Measurement of line current for another motor of the same model was used for verification of the **predicted** wave forms.

Further verification of the program can be seen in Figure 4.12 which shows the arc **duration** versus brush shift for different brush widths at **3200** rpm. This graph of data **from** the program shows minimum arc duration occurs at a brush shift of -5 degrees, that is 5 degrees opposite the direction of rotation for **3200** rpm and a **typical** automotive voltage level. This agrees with conventional DC motor design guidelines which indicate that a proper amount of brush shift against rotation improves commutation [47].

The mutually coupled arcing model output includes the i_a , and i_b wave forms and the **time** duration of the arc. The current i_b starts as the negative of i_a and is driven positively or negatively by the induced voltage in the "b" circuit path. After the mechanical commutation period the arc voltage works to equalize **the** current in the commutating coil with the current in the "a" circuit to which it is being switched. The direction and amount of brush shift determine the polarity and **magnitude** of the induced voltage in the shorted coil. Negative brush shifts produce induced voltage which helps to reverse the current in the **commutating** coil.

Differences between i_a wave forms output by this model versus the **less** sophisticated **models** only become apparent for the severe arcing conditions, **where** the mutually coupled current paths make a noticeable difference in the wave forms.

Brush Width Variation

The effective brush width increases as the motor "runs in." As the effective width increases, the current density in the brush drops and its life span is **extended**. However, the generated voltage produced by the motor rotating at a certain speed **drops** because of the reduction in average number of coils in the non-shorter current path. Figure 4.13 shows the result of effective brush width change on noncommutating current path wave forms. The **current's** DC level increases due to the reduced back voltage, resistance and **inductance** in the path. Initially, the i_a is distorted due to arcing. If there were no arcing then i_a current would just become less triangular and gain more harmonics as the brush **width** increased. A wider the brush contact means a higher **commutating** coil current as

shown in Figure 4.14, a longer arc duration as shown by Figure 4.15 and a narrow range of brush shift where the arc duration remains low.

Motor Speed Variation

The operating speed also has an effect on the current pulsation and commutation characteristics. The line current decreases as speed increases as shown by Figure 4.16. The commutating current, however, has the opposite effect as shown in Figure 4.17. This is because the commutating current is determined primarily by the back emf of the shorted coil, which increases with speed. The optimal value of brush shift moves toward zero as speed increases as seen in Figure 4.18, which shows a comparison of the arc duration for various brush widths at 2500 and 3200 rpm. This result is consistent with conventional wisdom in that the optimum commutation angle moves toward 0° as the load decreases [47].

Brush Shift Variation

Brush shifting is a practical and inexpensive means of reducing DC commutation arcing in small DC motors. For a given speed, a brush shift that is too negative to be optimal is called over commutation. Likewise, a brush shift in the positive direction from the optimal location is called under commutation. Figure 4.19 and 4.20 illustrate how the currents change as the brushes are shifted. When the motor is over commutated, at -10° brush shift as shown in Figure 4.19a, the i_a current wave form is noisy. The i_b wave form shown in Figure 4.20a shows that for over commutation the commutating coil current is reversed by the induced voltage in the coil. In this case the i_b current overshoots the i_a current at the point where commutation ends. This is not the case for the optimally brush shifted motor at -5° brush shift. For ideal commutation shown in Figures 4.19b and 4.20b, the i_b current is reversed by the induced voltage in the commutating coil so that when commutation ends there is little discrepancy between the i_a and the i_b currents. The under commutated wave forms shown for the $+10^\circ$ brush shift in Figures 4.19c and 4.20c, are full of harmonics and will cause increased noise in the current wave form. Under commutation occurs when the i_b current does not reverse during the commutation process and is driven to zero only when the arcing occurs. Because it helps to reduce the arcing, brush shift could also be useful in reducing radiated and conducted electromagnetic noise.

Further Research

Further research can be done into electromagnetically induced noise caused by the motor arcing using this model of commutation. The EMI properties of a given design may be better understood by examining the arcing conditions which exist.

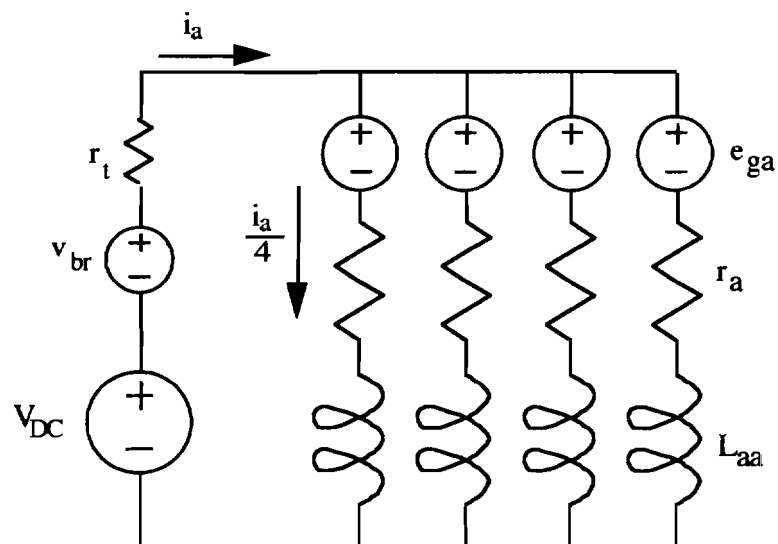


Figure 4.1 Stationary Circuit Model

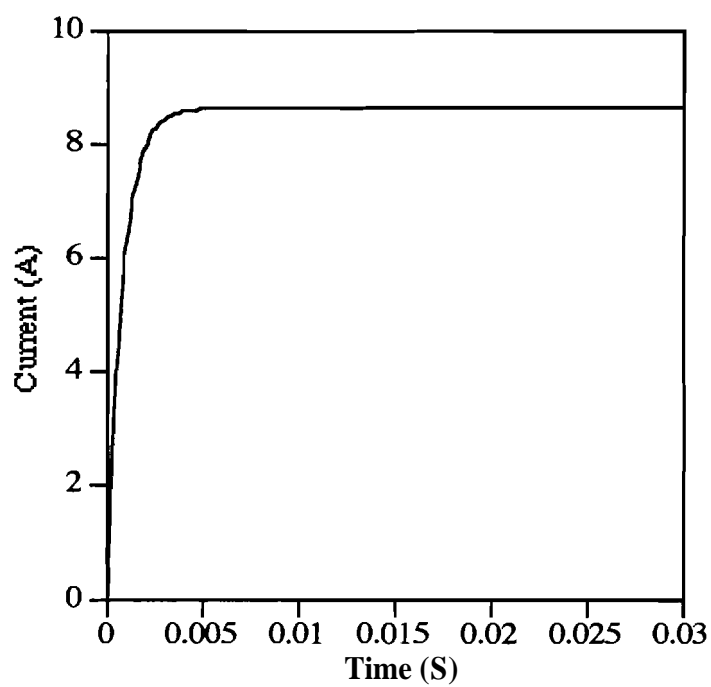


Figure 4.2 Stationary Circuit Model Current Output

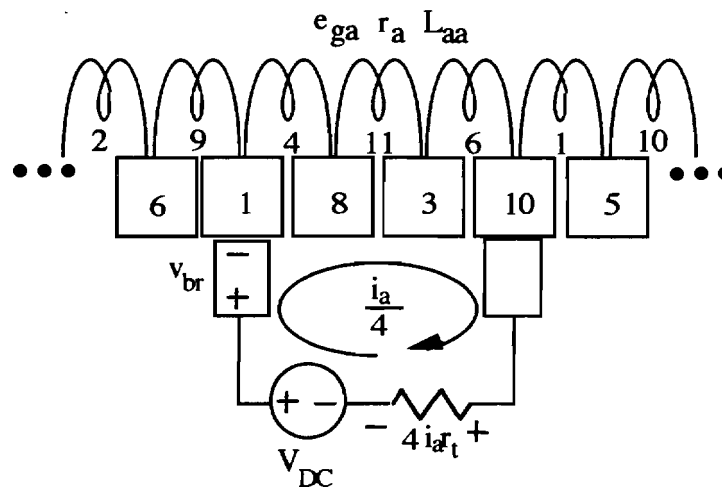
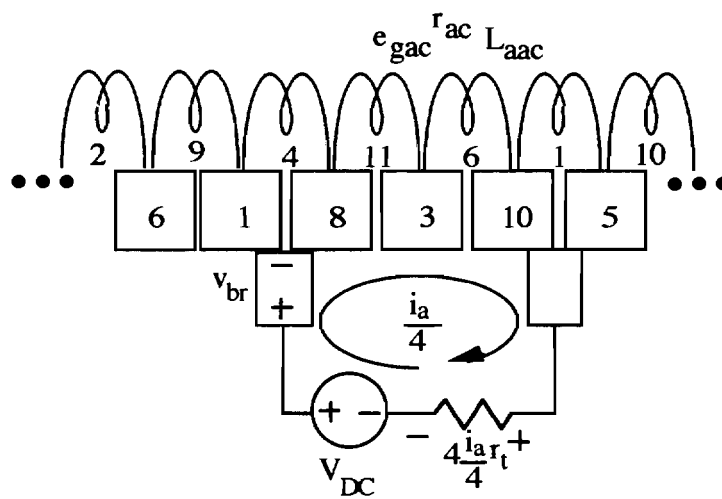


Figure 4.3 Circuit for Noncommutating Time Varying Model



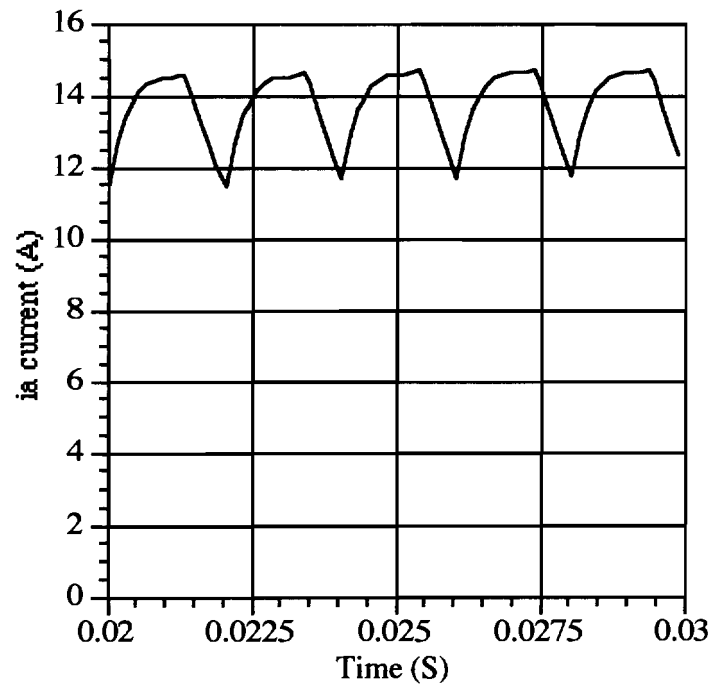


Figure 4.5 Time Varying Model Program Current Output

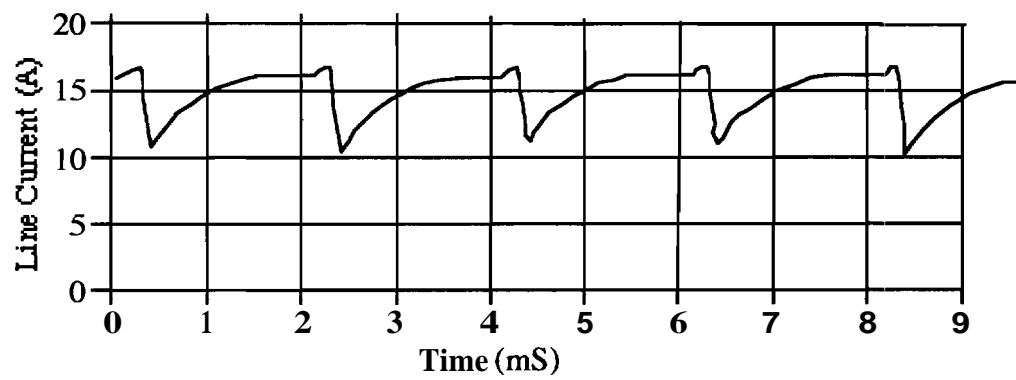


Figure 4.6 Measured Line Current

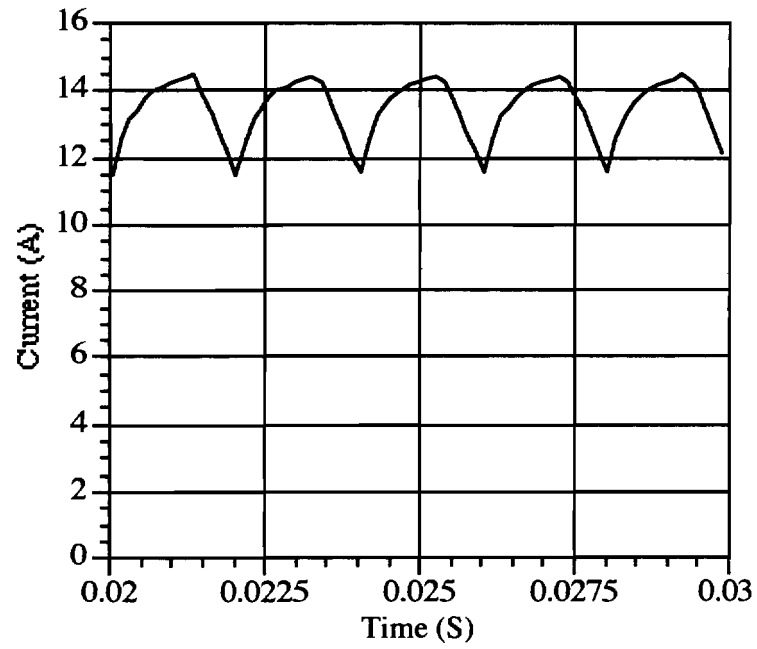


Figure 4.7 Line Current Predicted Using Position Dependent Inductance

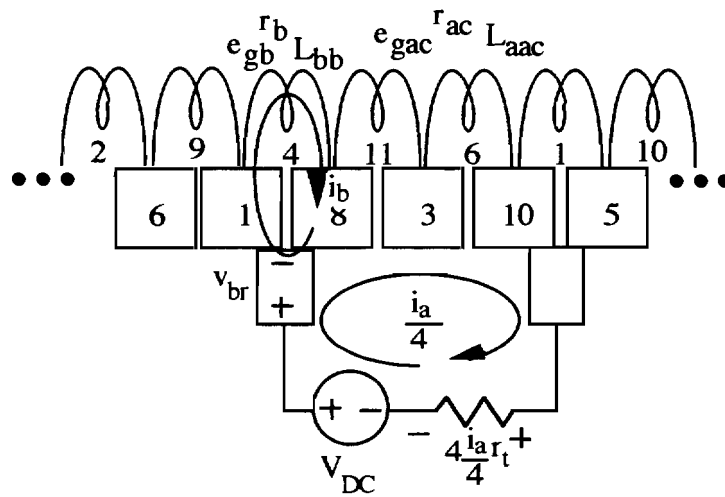


Figure 4.8 Mutually Coupled Commutating Circuit

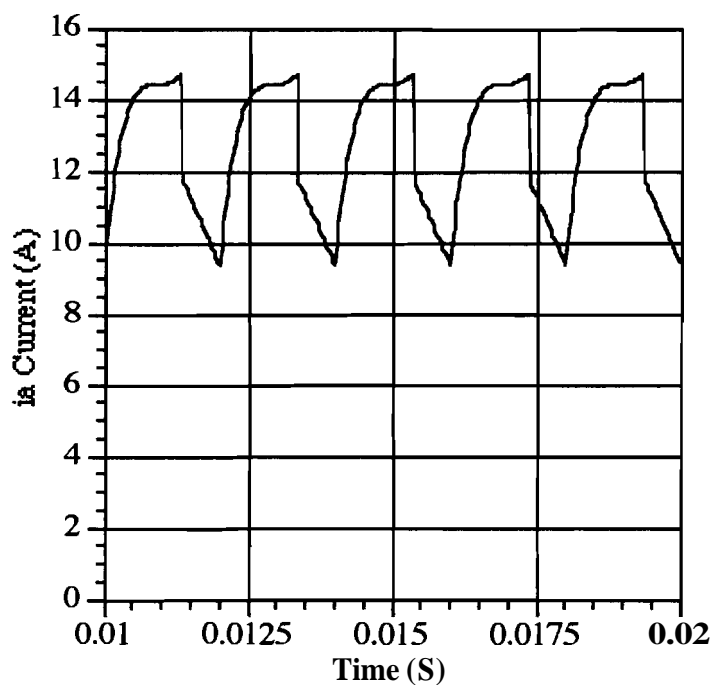


Figure 4.11 Commutation Arcing Model Line Current Prediction

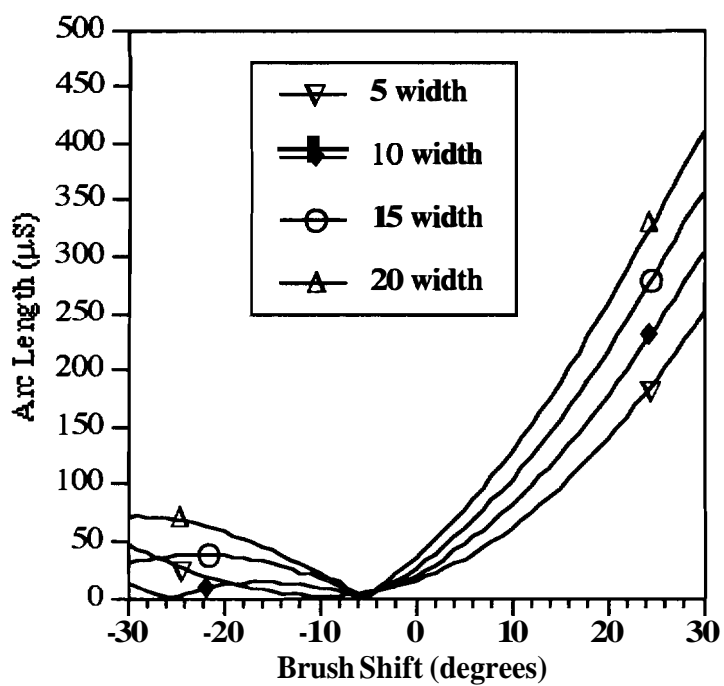


Figure 4.12 Optimal Brush Shift for Various Brush Widths

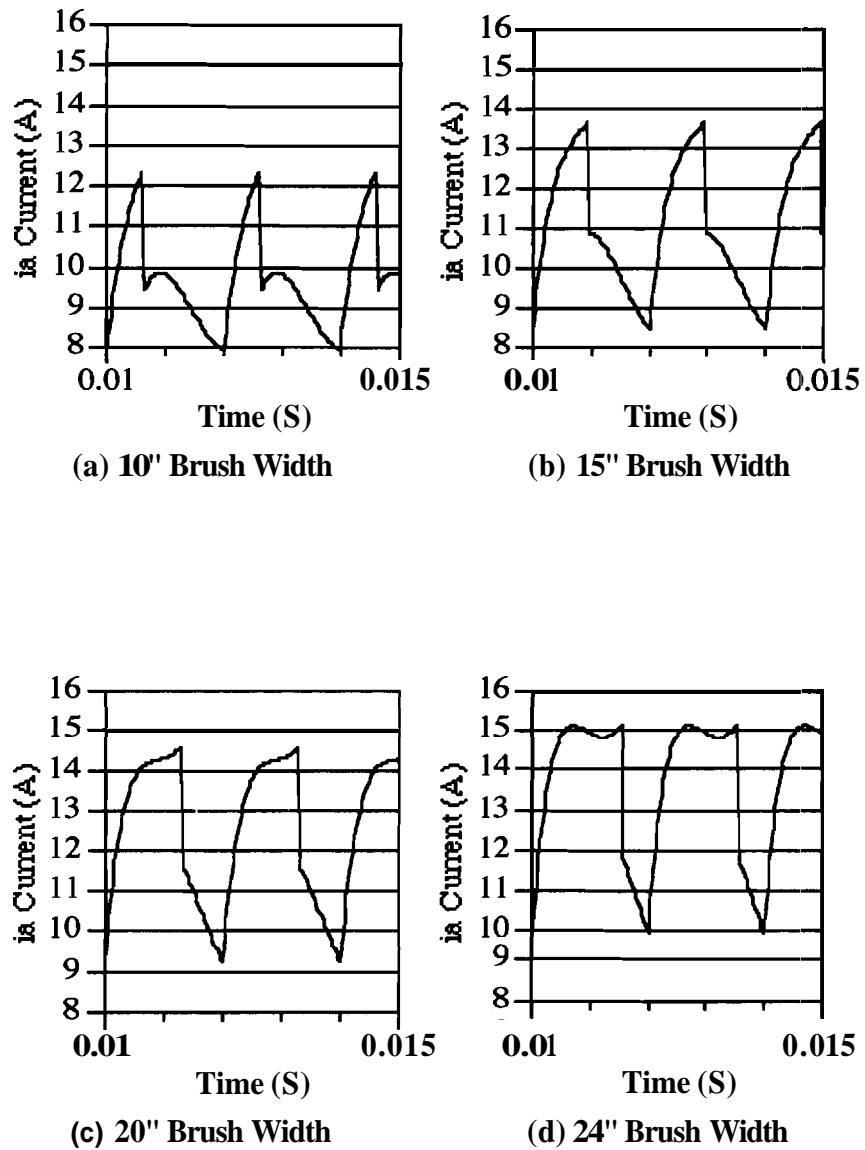
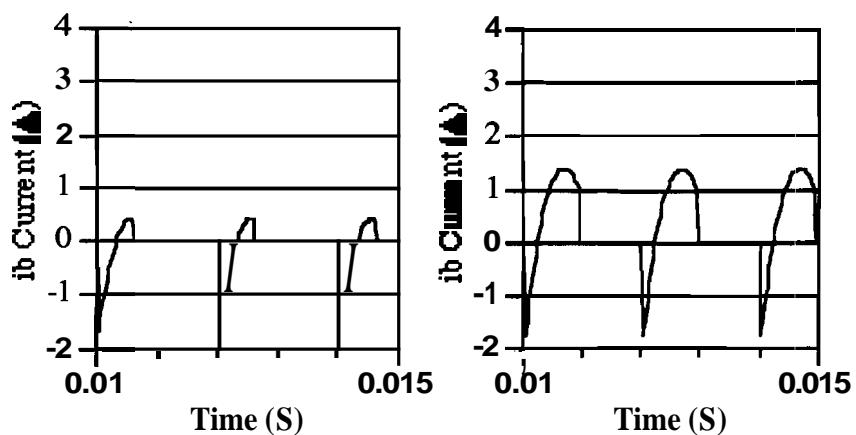
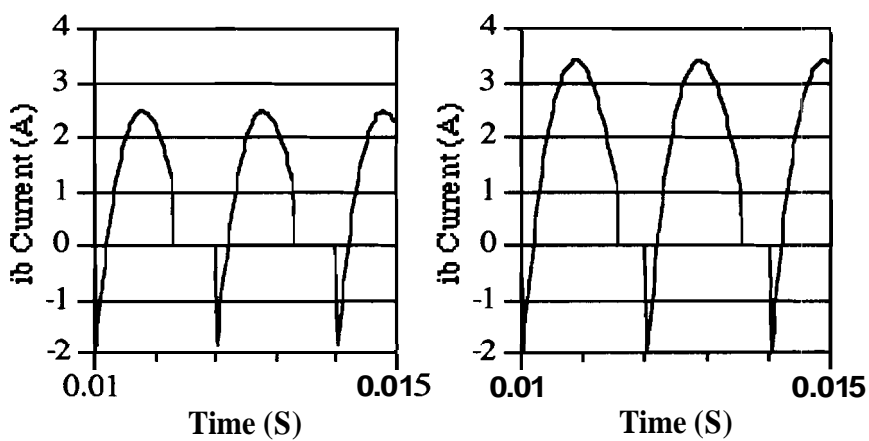


Figure 4.13 Line Current Wave Form Change with Brush Width Variation



(a) 10" Brush Width

(b) 15" Brush Width



(c) 20" Brush Width

(d) 24" Brush Width

Figure 4.14 Commutating Current Wave Form Change with Brush Width Variation

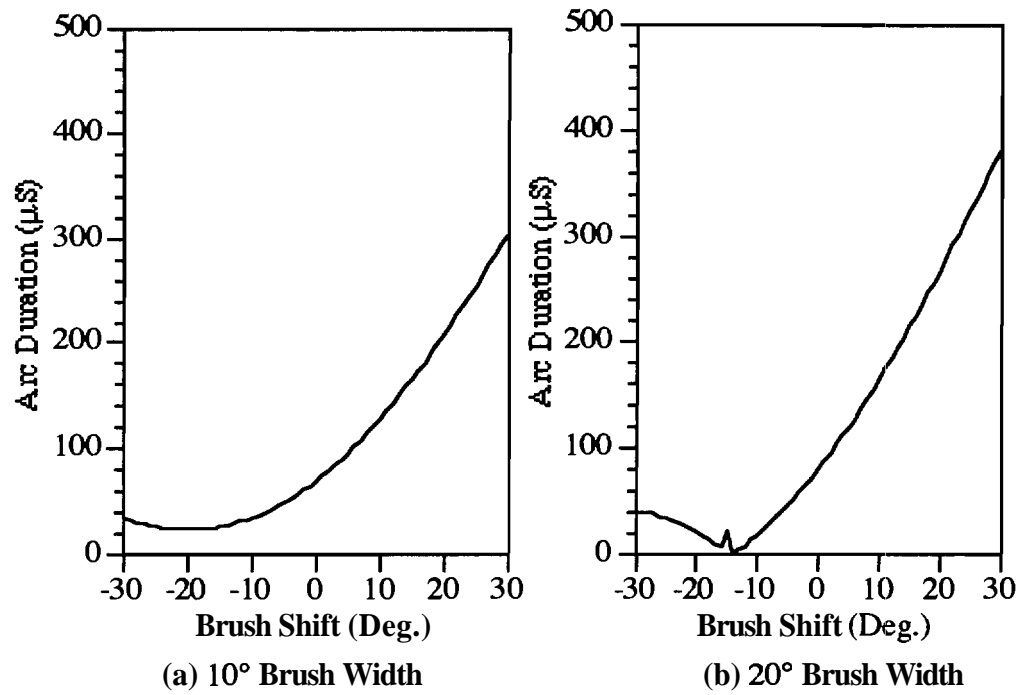


Figure 4.15 Arc Change with Brush Width Variation

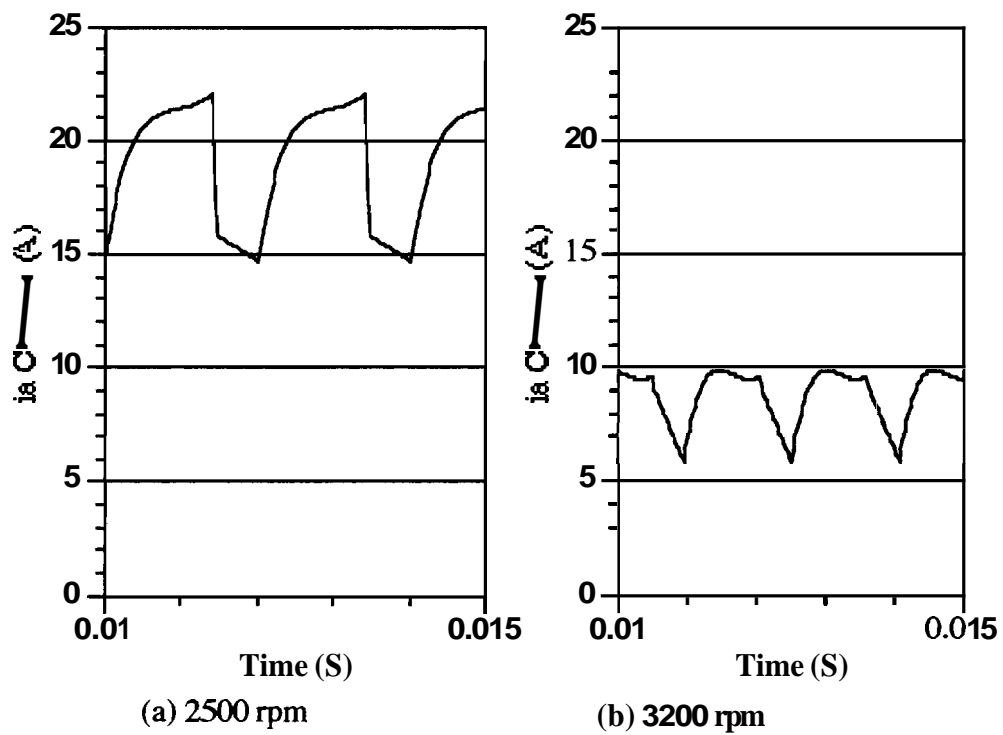


Figure 4.16 Line Current Change with Motor Speed Variation

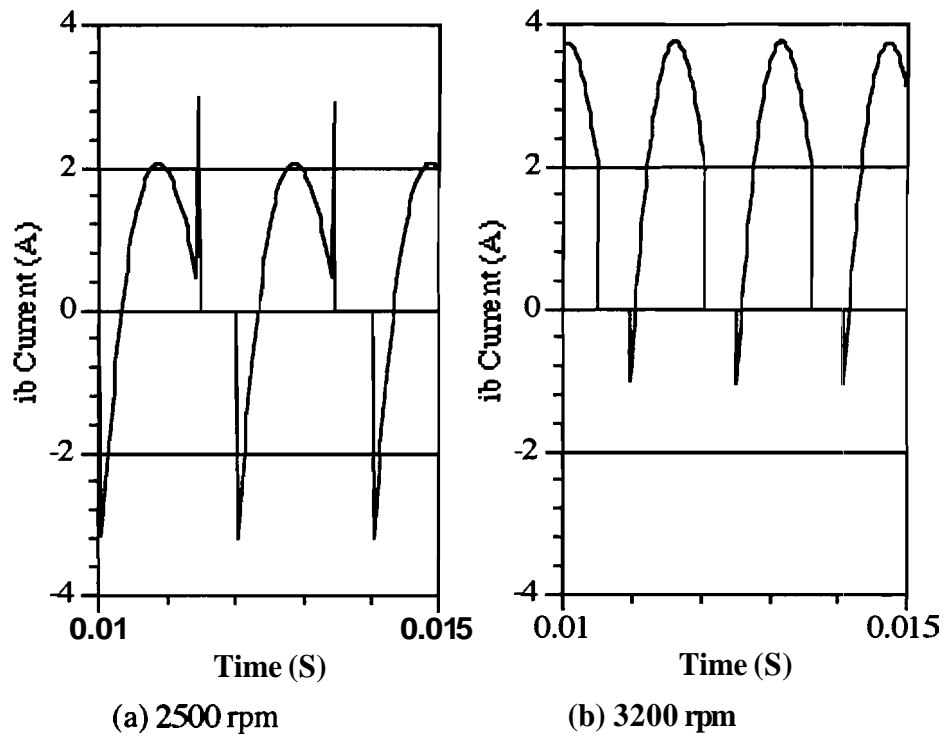


Figure 4.17 Commutating Current Change with Motor Speed Variation

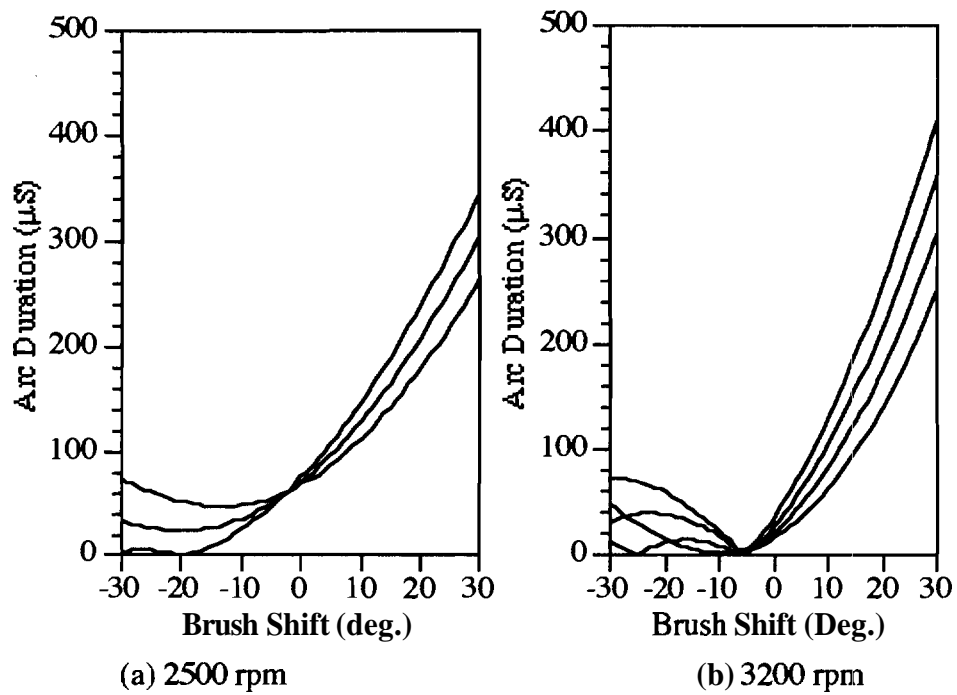


Figure 4.18 Optimal Brush Shift Change with Motor Speed Variation

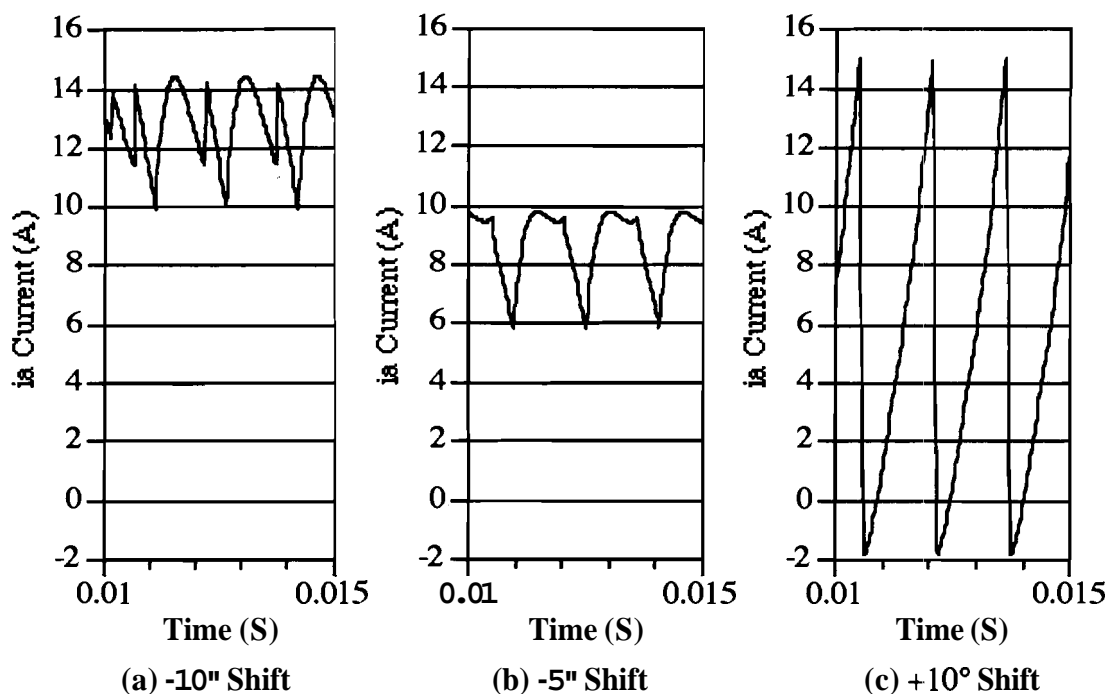


Figure 4.19 Line Current Wave Form Change with Brush Shift

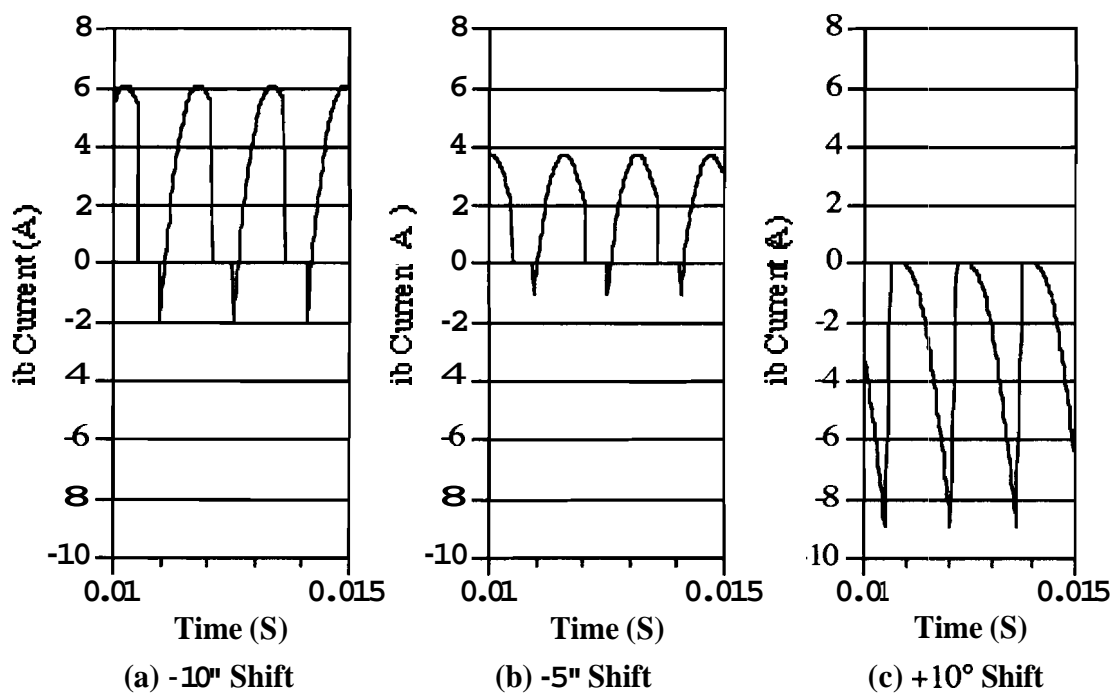


Figure 4.20 Commutating Current Wave Form Change with Brush Shift

CHAPTER 5. CONCLUSIONS AND FUTURE RESEARCH

Small DC permanent magnet motors which are lightweight, compact, and inexpensive, are well suited for low cost high production use in industry. Unfortunately, the audible noise emanating from these motors can cause a false negative perception of the motor's quality. In cars, for example, fan motor noise can be a nuisance. The objective of this thesis is to examine the connection between motor noise and the **line current** wave form for a specific four pole DC permanent magnet motor. It is further concerned with identifying the underlying factors which influence the **line** current ripple.

In Chapter 2 an audible noise to motor current transfer function is **determined** from test measurements and compared with a mechanical transfer function measured for the motor only and for the motor in the fan scroll assembly. The inductance, which is a factor in the shape of the current ripple, is computed from theoretical and empirical inductance functions in Chapter 3 . Finally Chapter 4 describes a sequence of progressively more complex models used to compute the current wave form.

Research Summary

Research accomplished for this thesis contributes to the study of permanent magnet DC **motors** in the following ways:

- 1.) A technique has been developed to measure the noise to motor line current transfer function.
- 2.) A comparison has been made of theoretical and actual inductance measurements in a permanent magnet **DC** motor.
- 3.) A model simulating commutation in permanent magnet DC motors has been developed which can be used to evaluate arcing phenomena. This arcing model can be used to determine the conditions **which** are detrimental to commutation.

Conclusions

An audible noise to motor current transfer function has been investigated and compared with the vibration to mechanical impulse transfer functions of the motor and scroll assembly. The peaks from the audible noise to motor current transfer function generally correspond to peaks observed in the mechanical transfer functions. This implies that interaction between the mechanical system and electrical system causes the motor noise. The noise level can be reduced by damping the mechanical structure with **added** mass or damping with **viscoelastic** polymers between the laminations or by eliminating unwanted frequencies from the motor current.

Having established the link between the coil current and some of the noise generated, this investigation proceeded to develop the tools for studying the coil currents, especially those undergoing commutation. First, the key parameters were **determined** for a detailed model that portrays the transient phenomena associated with commutation. Methods and problems related to the determination of the self and mutual inductance of the armature coil; were examined.

Next, a model of the motor was developed which includes the mutually coupled **shorting** current resulting from mechanical commutation and from the brief arc that generally occurs after the mechanical commutation. The model is shown to be reliable and can be used to predict optimal brush shifts and brush widths.

Future Research

Future research in the following areas based on the approach taken here will be beneficial:

- 1.) Use of the arc model to determine the nature of electromagnetic emissions from permanent magnet DC motors.
- 2.) Use of a spectral analysis of the current wave **form** from the model, with a modal analysis of the motor case to predict the level of noise. The noise associated with simulated current wave forms could be synthesized on a properly equipped personal computer.
- 3.) Use of the current to noise transfer function as a guide to check for possible problem frequencies before actual production of motors.

- 4.) Further refinement of the simulation models for use in predicting transient response.**

LIST OF REFERENCES

LIST OF REFERENCES

- [1] J.C. Gleadow, M. T. O'Brien, "Progress on the New Zealand HVDC upgrade," in *IEEE Conference Publication n 345*, pp. 138-146, Sept. 1991.
- [2] Zhi-qing Zhao, Yi-quan Yuan, "Recent Study of acoustic emission locating for partial discharge in UHV transformers and shunt reactors," in *Proceedings: Second International Conference on Properties and Applications of Dielectric Materials v 2 (of 2)*. Published by IEEE , pp. 634-637, Sept. 1988.
- [3] Dororn **Batan**, Isidoro Kerszenbaum, Jerome Frank, "Effect of core-clamp pressure on the sound level emitted by the cores of dry-type distribution transformers," in *IEEE Conference Record of Industrial and Commercial Power Systems Technical Conference*, pp. 101-106, May 1989.
- [4] John E. K. Foreman, Tom G. Onderwater, Eva M. Placko, "Assessment of audible noise from high voltage transmission lines and a high voltage transformer station," *IREsearch Report Canadian Electrical Association* , 77-27, November 1986.
- [5] G. A. Artocolo, "Root mean square response of Transducer systems to spectral density inputs," *SAE Technical Paper Series* , Paper 871748, October 1987.
- [6] Robert P. **Kendig**, S. E. Wright "Validation of acoustic intensity measurements for power transformers," *IEEE Transactions on Power Delivery* , vol. 6, no. 4, pp. 1524-1530, October 1991.
- [7] Robert P. **Kendig**, "Sound Intensity of the Comerford HVDC converter station," *IEEE Transactions on Power Delivery*, vol. 4, no. 3, pp. 1876-1881 July 1989.
- [8] Yvan Champoux, Blaise Gosselin, Jean Nicolas, "Application of the intensity technique to the characterization of transformer noise," *IEEE Transactions on Power Delivery*. vol. 3, no. 4, pp. 1802-1808, October 1988.
- [9] Arthur W. Kelley, "Measurement of spacecraft power transformer acoustic noise," *IEEE Transactions on Magnetics*, vol. 26, no. 1, pp. 281-289, Jan. 1990.
- [10] J. Roberts, "Principles of noise control with enclosures," *Journal of Electrical and Electronics Engineering, Australia*, vol. 10, no. 3, pp. 151-157, Sept. 1990.
- [11] I. Ya. **Eingorn**, " Magnetostriction of electrical steel and transformer noise," *Soviet Electrical Engineering (English Translation of Elektrotechniku)*, vol. 60, no. 4, pp. 28-30, 1989.

- [12] K. J. Dove, "Acoustic enclosures deaden transformer noise," *Engineering Digest* (Toronto), vol. 35, no. 5, pp. 45-46, October 1989.
- [13] Chinh T. Nguyen, Roger Beauchemin, "Program for calculating audible noise levels around power substations," *IEEE Computer Applications in Power*, vol. 3, no. 2, pp. 25-28, April 1990.
- [14] Samir N. Y. Gerges, Marcus A. Duarte Rogerio T. da Silva, "Fan Motors Noise Reduction," in *Proceedings: 1986 International Conference on Noise Control Engineering*, vol. 1, July 1986, pp. 131-134.
- [15] H. S. Sagoo, J. E. T. Penny, R. T. Booth, "Identifying noise sources in a vacuum cleaner," *Proceedings: 1986 International Conference on Noise Control Engineering*, vol. 2, July 1986, pp. 1211-1216.
- [16] W. R. Finley, "Noise in induction motors. Causes and treatments," in *Proceedings: 37th Annual Petroleum and Chemical Industry Conference*, September 1990, pp. 55-63.
- [17] Y. Hyodo, T. Konomi, "Application of superposition technique to vibration mode analyses using laser holography," *International Journal of Vehicle Design*, vol. 8, no. 4-6, 1987, pp. 504-513.
- [18] I. S. Glazunova, G. K. Lipskii, M. Yu. Pal'm, F. F. Yudin, "Study of noise and vibration in the motor-compressor unit of home refrigerators" *Vibration Engineering*, vol. 2, no. 1, 1988, pp. 27-33.
- [19] Alan K. Wallace, Rene Spee, Larry G. Martin, "Current harmonics and acoustic noise in AC adjustable-speed drives," *IEEE Transactions on Industry Applications*, vol. 26, no. 2, March-April 1990, pp. 267-273.
- [20] Ken'ichi Kimoto, Yukihiro Kameko, Kin'ya Hashimoto, "Decoupling control of an induction motor operated with a PAM inverter," *Proceedings: 19th Annual IEEE Power Electronics Specialists Conference*, April 1988, pp. 1091-1098.
- [21] Toshi-Hiro Nishimura, Takeshi Inoue, Mutsuo Nakaoka, Toru Maruhashi, "Magnetic force in three phase induction motor driven by ultrasonic carrier frequency sinusoidal PWM inverter," in *Proceedings: 19th Annual IEEE Power Electronics Specialists Conference*, April 1988, pp. 1069-1075.
- [22] Toshihiro Nishimura, Mutsuo Nakaoka, Toru Maruhashi, "Reduction of vibration and acoustic noise in induction motor driven by three phase PWM AC chopper using static induction transistors," *IEEE Transactions on Power Electronics*, vol. 4, no. 3, July 1989, pp. 313-318.
- [23] R. Belmans, W. Geysen, Ph-K. Sattler, R. Findlay, "Comparison of the audible noise level emitted by inverter-motor combinations," *Conference Record - IAS Annual Meeting*, Part 1 (of 2), October 1990, pp. 109-115.
- [24] Shinobu Aoki, Naosh Tsukiyama, "Low loss high gain 300V-200A class normally-off SIT module for DC motor control," in *Proceedings: 19th Annual IEEE Power Electronics Specialists Conference*, April 1988, pp. 703-708.

- [25] A. Kusko, S. M. **Peeran**, "Application of 12-pulse converters to **reduce** electrical interference and audible noise from DC motor drives," *Conference Record - IAS Annual Meeting* , Part 1 , October **1989**, pp. 438-449.
- [26] J. Crucq, "Theory and practice of acoustic noise control in electrical appliances," *Philips Technical Review*, vol. **44** no. 4, pp. 123-134.
- [27] V. A. Voronkin, V. Ya. Gecha, A. I. Kaplin, "Scientific problems of low-noise and low vibroactive equipment creation," *Soviet Electrical Engineering (English Translation of Elektrotehnika)*, vol. **60**, no. 4, pp. 28-30, **1989**.
- [28] A. Foggia, J. F. Maestre, J. C. Sabonnadiere, G. Reyne, J. F. Imhoff, "Control of mechanical vibration in DC machines," *Conference Record - IAS Annual Meeting* , Part 1 (of 2), October **1990**, pp. 99-101.
- [29] A. Roulhac de Rochebrune, G. Reyne, A. Foggia, "Prediction of vibration levels and resonant frequencies in static electrical apparatus" *IEEE* , **1990** pp. 122-127.
- [30] **Andrzej M. Pawlak**, **Tadeusz Glinka**, "Field Shape Influence upon Parameters of a DC mocromotor," *Electric Machines and Power systems* . , 1985, pp. 91-107.
- [31] James D. Jones, *Active Noise Suppression Notebook* , Class Notes, Purdue University, 1991.
- [32] Takayuki Suzuki, Takuya Kamano, "Modeling and Transient **Response** of DC separately excited motor taken account of armature reaction," in *Electric Machines and Power Systems*, **1987**, pp. .
- [33] Jaime De La Ree, Nady Boules, "Induced voltage harmonic **reduction** of PM cylindrical machines," in *IEEE*, May **1990**, pp. 152-156.
- [34] Nady Boules, "Prediction of No-Load Flux Density Distribution in Permanent Magnet Machines," *IEEE Transactions on Industry Applications*, vol. IA-21, no. 4, **May/June** 1985, pp. 633-643.
- [35] Nady Boules, "Two-Dimensional Field Analysis of Cylindrical Machines with Permanent Magnet Excitation," in *IEEE Transactions on Industry Applications*, vol. IA-20, no. 5, **September/October** 1984, pp. 1267-1277.
- [36] **Tomy Sebastian**, **Gordon R. Slemon** "Transient Modeling and Performance of Variable-Speed Permanent-Magnet Motors," in *IEEE Transactions on Industry Applications*, vol. 25, no. 1, **January/February** 1989, pp. 101-106.
- [37] R. S. **Ramshaw**, G. Xie, "Measurement of parameters of DC **machines**," *Electric Machines and Electronechanics* , 19, pp. 179-191.
- [38] Nady Boules, "Design optimization of permanent Magnet DC motors," in *Conference Record - IAS Annual Meeting* , October **1987**.

- [39] Jaime De La Ree, Nady Boules, "Magnet shaping to reduce induced voltage harmonics in PM machines with surface mounted magnets," *IEEE Transactions on Energy Conversion*, vol. 6,no. 1, March 1991, pp. 155-161.
- [40] Jaime De La Ree, Nady Boules, "Torque Production in Permanent-Magnet Synchronous Motors," *IEEE Transactions on Industry Applications*, vol. 25, no. 1, January/February 1989, pp. 107-112.
- [41] K. Padmanabhan, A. Srinivsan, "Some Important Aspects in the: Phenomena of Commutator Sparking," *IEEE PAS-84* May 1965, pp. 396-404.
- [42] John R. Suriano, *Simulation of Transients in Dirrect Current Motors*, Master's Thesis, Purdue University, 1986.
- [43] Conversation October 5th, 1992 with R. Belmans concerning experiments performed on DC motor used in submarine drive.
- [44] Conversation with R. Bernhard, September 30, 1992.
- [45] B. Hague, "Electromagnetic Problems in Electrical Engineering," Oxford University Press, London, 1929.
- [46] Ragnar Holm, "Theory of the Sparking During Commutation on Dynamos," *Conference Record - IAS Annual Meeting*, December 1962, pp. 588-595.
- [47] George McPherson, "An Introduction to Electrical Machines and Transformers," John Wiley and Sons, New York, 1981, pp. 390-391.